Check for updates

Recent progress in electrochromic energy storage materials and devices: a minireview

Devesh K. Pathak and Hong Chul Moon [iD] *

Integration of several functionalities into one isolated electrochemical body is necessary to realize compact and tiny smart electronics. Recently, two different technologies, electrochromic (EC) materials and energy storage, were combined to create a single system that supports and drives both functions simultaneously. In EC energy storage devices, the characteristic feature of EC materials, their optical modulation depending on the applied voltage, is used to visually identify the stored energy level in real time. Moreover, combining energy-harvesting and EC storage systems by sharing one electrode facilitates the realization of further compact multifunction systems. In this minireview, we highlight recent groundbreaking achievements in EC multifunction systems where the stored energy levels can be visualized using the color of the device.

1. Introduction

Electrochromic (EC) materials have attracted enormous attention since their discovery in 1961, and EC materials are used to regulate optical modulation (non-emissive dynamic displays) *via* redox reactions.[1–8] Their functional utilization in other related fields has rapidly developed in the past few decades.[9–11] In principle, the intercalation/de-intercalation of charge species by external stimuli alters optical modulation not only in the visible region but also in the infrared and ultraviolet (UV) regions, with possible applications in heat shutters.[12–15] In addition, the utilization of charge for coloration and bleaching in EC materials is useful in energy-saving systems.[16–18] Furthermore, the mechanism used for color switching could be recognized as the EC memory state of the device.[19–22] On the basis of these features, as well as fast response and low energy consumption, EC materials have significant potential applications in energy-saving glasses, smart windows, energy displays, EC electronic skin, information displays, and biological camouflage.[23–27]

Recently, much effort has been devoted to the synthesis of novel EC materials and designing them into a multifunctional device. Two technologies, namely EC materials and energy storage, have been combined into a single isolated EC energy storage system. A noticeable feature of this technology is the identification of the stored energy levels by color visualization, and the color intensity helps protect the device from overcharging.[28,29] In addition to capacitive or battery like materials, EC devices have also been integrated with photovoltaic materials and triboelectric/piezoelectric systems, where

Department of Chemical Engineering, University of Seoul, Seoul 02504, Republic of Korea. E-mail: hcmoon@uos.ac.kr

one electrode plays a dual role, and the novel features of this combined system have been explored for low power consumption.[30,31] However, several challenges in terms of development still exist. Additionally, it is equally important and highly desirable to design materials with multiple functions that will meet future requirements. Thus, researchers are continually striving to generate more reliable and efficient EC energy storage devices without compromising on individual quality parameters in one integrated system. In this minireview, we focus on the design of EC energy storage devices and their possible combinations for energy harvesting. The discussion concludes with new designs and approaches to working with existing challenges and future demands.

2. Materials and device fabrication

Chromophores, which are produced often under redox reactions, are the basic units for realizing chromic modulation in EC materials. Redox-active states are localized with respective color states and can be reversibly tuned by changing the polarity. The reversibility is often explained by faradaic reactions due to the charge intercalation/de-intercalation at the electrode–electrolyte interfaces which lead to a change in the oxidation state. This change in the oxidation state is seen as a change in color, and discharge under the reverse faradaic reaction (charge release) changes the color back to the natural state.[32–34] The surface architecture and electronic property of electrodes play a crucial role in increasing the reliability of a self-assembled EC energy storage system and improving its performance. Modified electrodes with nano-/microporous morphologies and high conductivity have been explored in a variety of inorganic and polymer
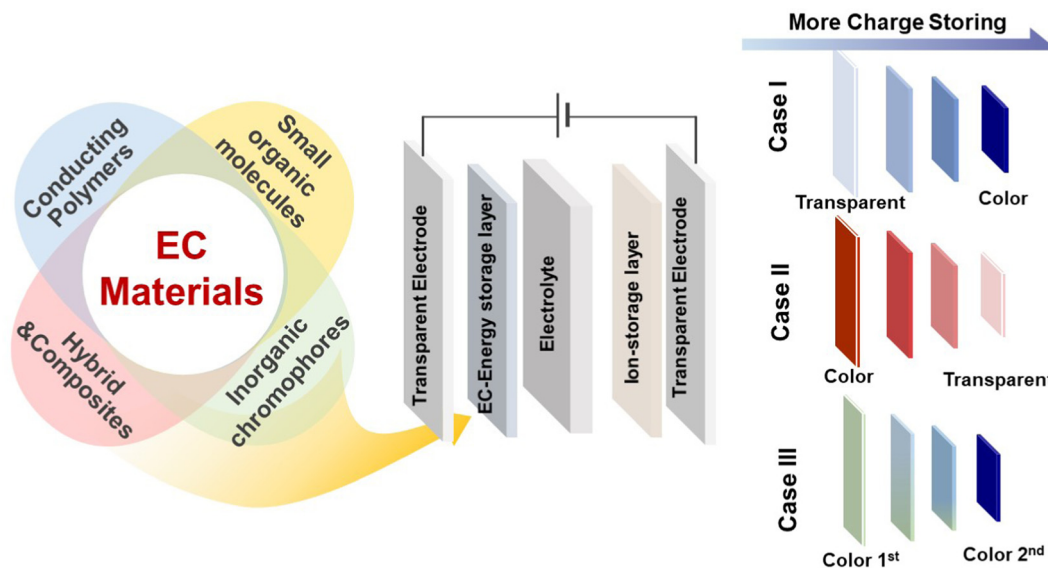
Fig. 1 Schematic illustration of the most common two-terminal EC energy storage device platform with three possible energy-dependent color changes.

materials.[10] However, most EC materials only show a limited palette of colors. Therefore, various conjugated derivative, hybrid and composite materials have been developed in EC energy storage devices in order to achieve different color states for measuring different charging levels by using different colors.[35]

Fig. 1 depicts a conventional EC device (in a two-electrode system) where the electrodes and electrolytes work together for an integrated capacitor or battery like system. In all EC device systems, external power produces chromophores at the electrode surface, creating energy-storing species. The stored energy level is easily visualized by the naked eye through adjacently placed transparent electrodes. Various conventional and novel materials from the EC family are used to create such a system where the materials are used either in the form of electrodes or in the form of electrolytes.

2.1 Small organic molecule

Viologens (V) constitute one of the representative small organic EC chromophores and they possess three reversible redox states: dication (V^{2+}), radical cation ($V^{+\bullet}$), and neutral form (V^0). The primary state of viologens, V^{2+}, is transparent and converts into an intense colored state ($V^{+\bullet}$) upon reduction. Viologen-based devices have been investigated due to their structural simplicity (electrode/EC/electrolyte/electrode), low-voltage operation, high optical contrast, redox stability, and color tunability by modifying N-substituents. The introduction of suitable counter anodic materials (e.g., ferrocene, ferrocene derivatives, hydroquinone, and tetrathiafulvalene) is crucial for higher performance and stability.[36–40] Otherwise, the coloration of viologens appears at a high external voltage where electrolysis of electrolytes occurs, leading to poor device stability.[41] Since all components are contained in one electrolyte layer, the diffusion of redox species should be considered. Usually, the diffusion of colored $V^{+\bullet}$ and oxidized counter material from the respective

electrode to the bulk electrolyte can induce undesired self-bleaching (i.e., self-discharging). Recently, the use of zwitterionic electrolytes has been proposed to reduce this diffusion issue and improve the shelf-life stability of viologen-based EC systems.[36]

The chemical structure of the viologen 4,4′-bipyridinium is always open for nucleophilic substitution from both sites.[42–44] Color tuning by virtue of the desired substitution is the main advantage of viologens in EC devices. The desired substitution of any group (symmetrically or asymmetrically), along with selective anionic species, tunes versatile chromic states in the newly derived viologen molecule. Various studies have reported on modified viologen molecules in different combinations of EC colors.[45] The desired chromic modulation of viologens mainly depends on the substituted organic groups, such as alkyl, aryl, and benzyl groups. In addition, functionalized viologens with polyionic liquids (PILs), cross-linked polymers, radical salts, phosphoviologens and triphenylamine-assisted ambipolar derived viologens have been explored for designing novel EC materials. These different viologen-conjugated systems define a clear change in the band-gap value with a lower value (0.5–3.0 eV) and possess a variety of color states.[46,47]

However, viologen moieties always work as a charge-trapping layer for all kinds of substituent groups, with a significant decrease in the driving voltage for their respective chromic modulation or with faster switching kinetics due to improved conductivity.[48] Recently, ionic liquids have replaced the liquid electrolyte medium and play a bifunctional role as an ion and a solvent simultaneously. The extraordinary properties of ionic liquids, such as high conductivity, large operating potential range, nonflammability, high boiling point, and strong compatibility with most organic solvents, enable the formation of a most suitable composite with viologen molecules. Moreover, PILs have properties of both polymers and ionic liquids and, therefore, exhibit their immobilized electroactive species as a

viologen in an electrolyte medium. PILs slow down the recombination reaction, improving EC material performance; therefore, ionic liquid electrolytes are increasingly used in multifunctional applications of viologen-based EC devices.[49–51]

2.2 Conducting polymers

Conducting polymer (CP)-based EC systems exhibit their EC modulation in the form of thin films. We note that CPs are also categorized as organic systems. However, their operation principles including the device configuration and state of the EC layer are different from those of viologen-based single-layer platforms, so we describe CP-based systems separately. CPs have a delocalized π-electron band structure, and the dynamic electrochemical doping/de-doping process determines their EC properties *via* changing the optical band gap.[52,53] CPs show distinct optical changes and vivid EC colors in the visible range. The EC performance of the device with CPs includes advantages of wide color diversity, fast switching speed, and low self-bleaching. However, the optical contrast is relatively lower than that of the viologen-based device.

All electrochromically active polymers, such as polyaniline (PANI), polythiophene, polypyrrole (PPy), and their derivatives, exhibit EC performance as thin films once the electrode (or film) is used for a redox reaction. During the redox reaction, doping and undoping of counter ions determines the unique optical characteristics that are governed by the delocalization of π-electrons in the energy band of the material structures. Therefore, a change in the gap between the highest occupied molecular orbital (HOMO) and the lowest unoccupied molecular orbital (LUMO) imparts to them their intrinsic EC properties. A change in the spectral properties in terms of color tuning is achieved by selecting appropriate substitutes and highly depends on the length of the polymer chain. For example, a methyl group in 3-methyl thiophene allows a possible color state of pale blue, blue, and violet in its oxidized form and purple, yellow, red, and orange in its reduced form. Similarly, the alkyl-substituted thiophene poly(3,4-ethylenedioxy thiophene) (PEDOT) provides a lower band gap, compared to its individual constituents, and is recognized by its two-color state of blue/black (neutral state) and transparent (oxidized state), while polythiophene shows apparent EC color switching from its original magenta to a transparent color with oxidation.[6,54]

Recently, Ming *et al.* developed a D–π–A–π–D-type conjugated polymer. 3,4-Dihexoxythiophene was used as a π-spacer to design a conjugated polymer, poly(4,7-bis(5-(2,3-dihydrothieno[3,4-*b*]-[1,4]dioxin-5-yl)-3,4-bis(hexyloxy)thiophen-2-yl)benzo[*c*][1,2,5]thia-diazole) (poly(BT-ThEDOT)). The modified D–π–A–π–D-type polymer showed lower oxidation by exhibiting a blue color instead of its neutral green.[55] Different electron donor and acceptor molecules have been used in polymer synthesis and exhibit versatile color states, with better conductivity for charge transportation and better performance.

2.3 Inorganic materials

Metal oxides and inorganic–inorganic composites are categorized as inorganic EC materials and exhibit optical modulation through the d-level splitting of transition metal atoms by virtue of the intercalation/de-intercalation of ions in an electrochemical cell.[1] Since the intercalation of ions into the thin film is generally limited, modifying the surface structure leads to improved EC performance. Inorganic nanostructures can easily be synthesized, which provide more active sites that facilitate ion diffusion, resulting in a high optical contrast.[56,57] High stability even under light (UV) exposure, long-term durability, and a wide range of operating temperatures are common advantages of most inorganic EC materials. However, the achievable EC color from the inorganic system is relatively limited to bluish and brownish.[58,59]

Optical modulation in blue and black color states is generally achieved with NiO, WO_3, TiO_2, and Prussian blue during a change in the oxidation states at the electrode surface, while V_2O_5 is known for EC color switching from gray to yellow. Like CPs, a solid thin film-based electrode is required for inorganic EC modulation. Changing the oxidation states of these metal atoms at the electrode surface changes the band gap, leading to a color change. However, to achieve higher optical contrast, the device prepared using inorganic materials needs high power input and shows low efficiency for coloration. Despite the change in color, electrochemical performance is determined by the thickness of the film, composition, and metal doping. Such changes tailor the charge transfer mechanism for better EC performance.[60–62] Since every EC property is governed by the faradaic reaction, inorganic materials also show a reversible color change with recombination of oppositely polarized species, either by providing a reverse voltage or by self-diffusing under an open-circuit condition.

In addition to derivative inorganic materials, different nanostructures of transition metal electrodes are most promising materials with better EC performance. Recently, a 2D titanium carbide (known as MXene) thin film synthesized by Pol *et al.* showed a reversible shift from the green to the blue color state of metal electrodes, and their color states could be tuned by varying the surface functionalities of $Ti_3C_2T_x$.[63,64] Even beyond chromism, inorganic materials are also combined with organic materials such as viologens and CPs for use as counter electrodes to improve the overall performance of EC devices. Therefore, a transition metal-based EC device shows a fast response and higher efficiency without the support of counter ion species.[65]

2.4 Hybrid and composite materials

The combination of organic and inorganic materials offers high thermal and chemical stability, and it has the potential to prevent structural damage. Due to their redox properties, inorganic EC materials can be used for counter electrodes when combined with organic or inorganic EC materials. It is important to distinguish between the inorganic and organic phases since they interact differently in a combined system.[66] The hybrid materials are formed by a strong chemical interaction *via* interfacial ionic or covalent bonds, whereas the composite materials are formed due to physical contact between the inorganic and organic phases through a weak interaction such as hydrogen bonds and van der Waals forces.

The characteristics of inorganic materials (*i.e.*, short ion diffusion length) and organic materials (low band gap, color tuning and fast switching) improve long-term stability, optical contrast and fast switching time in their thin solid film electrode geometry.[67,68] Designing a composite structure with large interfacial areas and strong interactions is crucial for achieving synergistic effects between organic and inorganic phases. Many strategies, such as incorporating compatibilizers (organic acids) for providing inter-chain metal charge transfer leading to less resistance and preparation by layer-by-layer (LBL) assembly for large areas and strong interfacial interaction, have been deployed recently for designing EC active electrodes.[69,70] An LBL nanocomposite thin film assembly reported by De-Long *et al.* with a PANI/PB structure exhibited a fast response (<1.5 s) and high optical contrast (61.1%).[71] Zhu *et al.* synthesized WO_3 nanoparticles by using chlorosulfonic acid to serve as a charge transfer center in poly(*p*-phenylenebenzobisthiazole), which improved the contrast. Similarly, the core–shell structure of WO_3/PEDOT enhances the charge transfer process and therefore reflects a quick hike of 50% improved optical contrast.[72] Zhang *et al.* reported an inorganic–organic composite of WO_3-PANI which improved the electron transfer kinetics, resulting in the EC switching time of 0.9 s from 5 s in the case of pure WO_3.[73] Researchers have found high EC coloration efficiency in the combination of PEDOT:PSS/WO_3, PEDOT:PSS/$W_{0.71}MO_{0.29}O_3$, PEDOT/V_2O_5, antimony doped tin oxide/PANI and in many other such composite structures.[74–76]

Moreover, interfacial covalent bonds are also investigated to enhance interchain electron transfer and modulate donor–acceptor interaction between organic and inorganic phases to facilitate ion transport in EC hybrid materials. This is much required because the kinetics of chromic modulation in EC polymers is controlled by ion diffusion. For realizing such characteristics, a star-like geometry of compact crystalline structures of hybrid materials has been synthesized by researchers.[77,78] The star-like approach in multilayer thin film of the POSS(polyhedral oligomeric silsesquioxane)-PANI/poly(2-acrylamidomethane-2-propanesulfonic) hybrid structure shows much higher contrast under dynamic switching conditions. The covalent approach has also been extended to prepare SWCNT-PANI hybrids.[79,80] In addition to this, a new class of porous crystalline metal–organic framework (MOF) materials, where the inorganic and organic phases refer to the metal source and organic ligand respectively, illustrate a ligand charge transfer process at the low potential value in hybrid materials. MOFs still face challenges with their insulating nature; however, the introduction of redox-active organic linkers improves charge-transfer properties, resulting in better performance.

Moreover, the transition metal complex system produces an additional absorption band, leading to other colors, due to the existence of metal-to-ligand or ligand-to-metal or d–d transition characteristics.[81,82] Synthesis and solubility problems are often exhibited in these complex structures due to the high molecular weight conjugated polymer containing the transition metal. However, Cu(II) and Fe(II) based metallo-supramolecular polymers with an aromatic azo ligand confer good solubility to the metal complex for the preparation of metallopolymers using polycondensation.[83] Therefore, Sergiusz *et al.* designed a series of polyazomethine metal complexes with Fe(II) and Cu(II) metal ions by on-substrate polymerization, exhibiting a color change from orange to grey and yellow to blue respectively.[84] Color-to-color transitions are sometimes influenced by thin film electrodes with different ligand structures and porosity. Indulekha *et al.* designed Fe(II)–terpyridine metallopolymer for a tunable capacitive response with supercapacitive properties.[85] Recently, one more complex material, two-dimensional coordination nanosheets (CONASHs), has attracted much attention because of its tunable chemical and physical properties, high ion mobility and excellent mechanical stability. CONASHs have also been found to be attractive for making NIR active multicolored EC displays and show excellent performance for long cycles.[86,87] Because of their two-dimensional lateral network, the in-plane and internanosheets show anisotropic charge-transfer behaviors, resulting in improved charge storage performance when compared to conventional metal complexes with a one-dimensional structure.[88,89]

2.5 Device operation and approach

EC device manufacturing is easy, where two electrodes (ITO/FTO) are assembled in crossbar geometry with a suitable electrolyte, as shown in Fig. 1. EC devices are analyzed in two detection modes, transmission (for smart glasses and windows) or reflecting (displays) mode. An EC device is developed into a five-layer system with two transparent conducting layers, one ion storage layer, one electrolyte layer, and one EC layer. The EC layer at the electrode and the ion storage layer together serve as the working and counter electrodes, respectively, while the electrolyte layer mainly creates a transmission channel for ions (Li^+, Na^+, K^+) under external electrical biasing. A higher conductivity of electrolytes leads to better performance of the EC device. Since a traditional EC device is highly brittle, EC devices are now being designed in flexible, stretchable, and foldable geometries to increase effectiveness. Different polymers, such as polyurethane (PU), butadiene rubber (SBR), natural rubber (NR), and poly(dimethylsiloxane) (PDMS), are used.[90,91] These substrates are made conducting by performing metal/nanometal conductor- and CP-assisted electrode fabrication using silver nanowires (AgNWs), carbon nanotubes (CNTs), graphene, poly(3,4-ethylenedioxythiophene) polystyrene sulfonate (PEDOT:PSS), and PPy materials. However, the chromic modulation mechanism in such devices is still the same as in traditional devices.

In a device that combines EC and energy storage functions, the standing charge level is anticipated by displaying the color state and such a device is generally referred to as an EC energy storage device. Studies have investigated a set of inorganic, organic, and polymer materials and their hybrid device structures to design such functional devices. Fig. 2 depicts the recent research intensity in different types of EC energy storage devices, where the height of the bars indicates the level of research. In energy storage systems, various EC materials have not only been functionalized to design electrochromic supercapacitor (ECS) and electrochromic battery (ECB) systems but
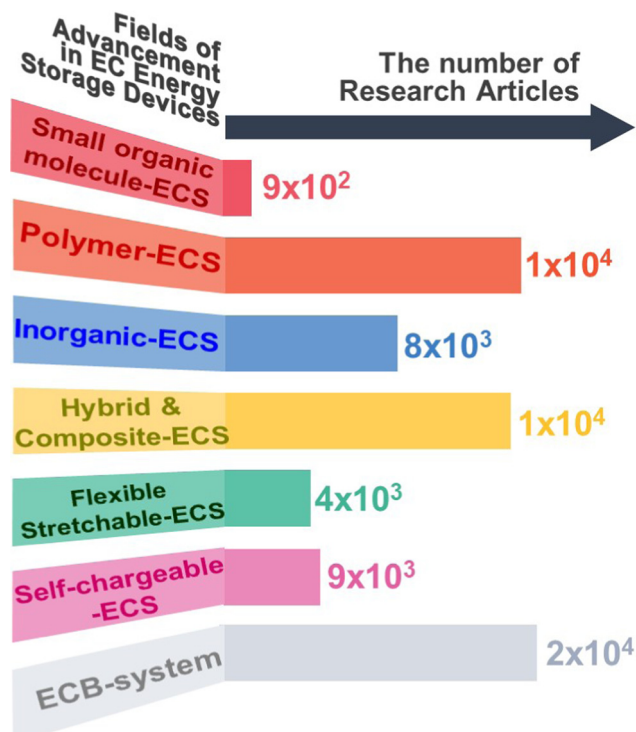
Fig. 2 Intensity profiles of recent EC energy storage systems. EC: electrochromic; ECB: electrochromic battery; ECS: electrochromic supercapacitor. Searching keywords (searched date August 2022) from Google Scholar; for all above device structures (top to bottom): viologen electrochromic supercapacitor, conducting polymer electrochromic supercapacitor, inorganic electrochromic supercapacitor, hybrid and composite electrochromic supercapacitor device, flexible stretchable electrochromic supercapacitor device, self-powered electrochromic supercapacitor, and electrochromic battery.

also have gained an extraordinary advantage in self-charging devices for energy-harvesting systems.[16,92,93] In addition, ECBs and hybrid and composite based ECSs have been equally explored in recent years, while few studies have been conducted on the small organic molecule based (viologen based) ECS system. There have been many attempts to improve device performance with different color combinations; however, this minireview only focuses on recent achievements in EC energy storage systems rather than the detailed mechanism of the functioning of chromic modulation and energy storage separately.

3. Electrochromic energy storage devices: EC supercapacitor

With the advent of nanomaterials, energy storage devices (capacitors) with ultrahigh capacitance have been extensively explored in academic and industrial areas. High energy density, fast charging/discharging, and low equivalent series resistance, compared to other energy storage systems, are the major advantages of supercapacitors. The operational mechanism of a supercapacitor depends on two basic principles of charge storage: physical adsorption of charges at the electrode surface and storage in the mixed-valance redox state defined by electric double-layer

capacitor (EDLC) and pseudocapacitor, respectively.[94,95] Numerous EC materials have been investigated for designing ECSs, where the electrochromically active material is used either in a single-layered form between two electrodes or in a thin-film form at the electrode surface. Here, we highlight viologen, inorganic, polymer, hybrid and composite materials for ECS devices that exhibit bifunctional applications when designed properly with a suitable electrolyte channel.

3.1 Small organic molecule-based ECSs

Although the diversity of colors in various modified viologen structures has been explored over the years, no literature is available on viologen based ECSs. Some studies have investigated the capacitive property of viologen molecules but have not highlighted its simultaneous effect with chromic modulation. Sethuraman *et al.* reported that a single redox-active viologen (1,1′-diethyl-4,4′-bipyridinium bromide)-based molecule mixed with 1 M H_2SO_4 improves capacitive performance, when combined within charcoal-based conventional electrodes, because of the redox behavior of bromide and 1,1′-diethyl-4,4′-bipyridinium ions.[96] The presence of cationic and anionic species in viologen molecules leads to a maximum capacitance of 408 F g^{-1} at a current density of 0.25 A g^{-1}, which is higher compared to the neat electrolyte (H_2SO_4) and triethylbutylammonium bromide (N2224Br) electrolytes. It means that viologen develops a π–π interaction at the carbon electrode surface and leads to the development of an EDLC ion layer; therefore, the system acquires a higher capacitance. In addition, the zerovalent viologen inhibits the capacitive property due to its insoluble ability in an aqueous medium. To resolve this issue, the 1,1′-bis[3-(trimethylammonio)-propyl]-4,4′-bipyridinium (NV^{4+}) molecule, which transforms into an NV^{2+} redox state by accepting two electrons and shows high solubility in an aqueous solution, is used.[97] The redox property is due to the presence of electrolyte viologen (NV^{4+}/NV^{2+}; act as an anolyte) and bromide (Br; act as a catholyte) ions. To solve the cross-diffusion issues of these species, the tetrapropyl ammonium cation (TPA^+) and the quaternized styrene ethylene butylene styrene membrane (SEBS-QA) are used to make a complex with the Br^{3-} anion and the NV cation, respectively. The formation of an $NV^{4+}/TPA^+/Br$ electrolyte with the SEBS-QA membrane in overall geometry results in appreciable performance toward energy and power density. However, these studies did not investigate any EC property of the viologen, along with energy storage characteristics.

Jang *et al.* attempted to fabricate a single-layered viologen-based ECS device.[98] The device was fabricated using $EtV(PF_6)_2$ and the anodic counterion species dimethyl ferrocene. Both were mixed in an ionic liquid 1-ethyl-3-methylimidazolium bis(trifluoromethylsulfonyl)imide ([EMI][TFSI]) and a random copolymer gelator poly(styrene-*ran*-methyl methacrylate) (PS-*r*-PMMA) to prepare a solid electrochromic electrolyte. The fabricated device, shown in Fig. 3a, contained a single layer of electrochromically active material sandwiched between two ITO substrates. The device showed a dark-blue color upon charging and became transparent upon discharging at a certain current density. However, the device geometry did not fully recover its initial optical characteristics, even
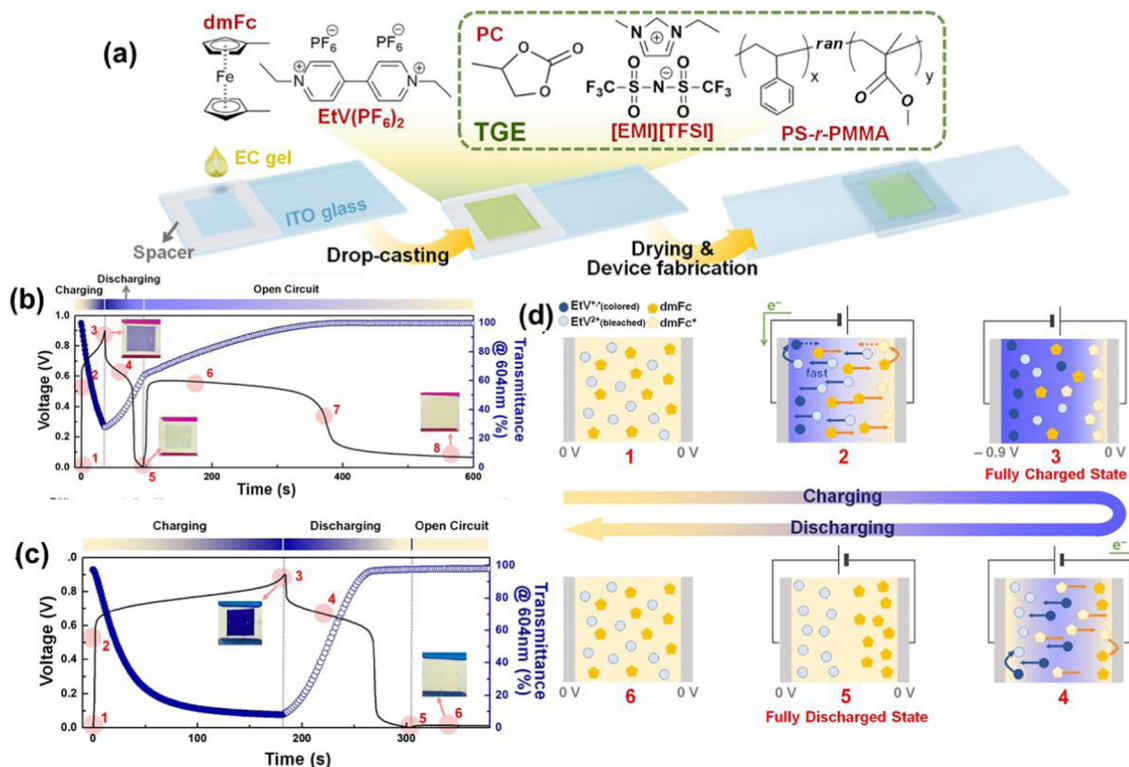
Fig. 3 An ECS device structure carrying single-layer viologen with a TGE electrolyte (a). Synchronized transmittance of the device with different possible states of charging–discharging functions of TGE-0 (b) and TGE-45 (c). Operating mechanism of a TGE-45-based ECS in six different steps (d). ECS: electrochromic supercapacitor; TGE: ternary gel electrolyte. Reproduced from ref. 98. Copyright [2021] Elsevier.

after achieving a cell potential of 0.0 V upon discharging, and the cell potential was surprisingly reinstalled at 0.57 V under the open-circuit condition, as shown in Fig. 3b. Therefore, the device showed delayed self-discharging to return to its initial color state. To resolve this unusual trend of charging–discharging of electrochromic ionic species, a binary liquid system containing [EMI][TFSI] and polycarbonate was mixed with the same solid electrolyte, named ternary gel electrolyte (TGE). A selective concentration of TGE-45 showed high conductivity (5.84 mS cm^{-1}) and elastic modulus (62.4 kPa). TGE-45 supported the diffusion of faradaic charge species of viologen and ferrocene and therefore did not leave any unusual residual charge species at 0.0 V during discharging, as shown in Fig. 3c. The device did not show a significant open-circuit voltage after complete discharging, and therefore, completely recovered its initial color state, showing high optical contrast ($\Delta T \approx 94\%$). Typically, a high capacitance (6.3 mC cm^{-2}) was observed, compared to the ionic gel, with the TGE-45-based single-layer electrolyte. This is due to the diffusion-controlled mechanism between the redox-active species and can be understood with the help of a cartoon representation of the ECS device mechanism,[99,100] as shown in Fig. 3d. During the charging state of the device, TGE-45 contributes to quick accumulation of both redox-active species (EtV^{2+} and dimethyl ferrocene) at the electrode surface, leading to an intense deep-blue color. Therefore, many redox species are used to obtain an intense deep-blue color and more charge storage with a longer charging time. Fast ion transportation is

not allowed for complete neutralization of the redox species with TGE-0 during discharging. During discharging with TGE-45, controlled diffusion of the redox-active species occurs, and full energy consumption is achieved with high capacity. Complete recovery of the redox-active species in its neutral form restores the original transmittance. The diffusion of mass transport redox species follows Fick's law in a single-layer viologen-based ECS, reported recently by Seon *et al.*[101] Residual charges that are generally not extracted under normal discharging conditions and left over in the cell were examined and were found to be responsible for suppressing energy storage. Therefore, the concentration gradient during device fabrication could help extract the maximum stored energy by reducing residual charges.

3.2 Conducting polymer-based ECSs

In contrast to the limited reports on viologen-based ECSs, there are a variety of active polymers whose color-to-colorless and color-to-color switching has been examined for ECS devices. The molecular structures of CPs are easily controllable for bifunctional activity and lead to improved capacitance due to their optimized morphology.[102–104] Recently, there have been many attempts to design conjugated polymers with donor (D) and acceptor (A) units, called D–A and D–A–D type polymers, which exhibit wider absorption spectra due to intermolecular charge transfer among these units and therefore show different colors. Modulating the donor and acceptor units is an effective approach to designing a series of CPs.[105,106] The first neutral

green color of a CP was obtained by Sonmez *et al.*, who synthesized a polymer using thiophene (donor) and thieno[3,4-*b*]pyrazine (acceptor) units.[107] The similar polymer unit affected ionic transport channels and was especially noticeable in thicker films for suppressing performance.

A π-spacer was introduced between donor and acceptor units (D−π−A−π−D-type polymer) and the polymer was shown to display excellent optical properties and device performance. A D−π−A−π−D-type polymer, shown in Fig. 4a, with 3,4-ethylene-dioxythiophene (EDOT), benzo[*c*][1,2,5]thiadiazole (BT), and 3,4-dihexoxythiophene as donor, acceptor, and π-spacer units, respectively, was designed for ECSs.[55] Three main factors in this system contributed to high performance: (1) a noncoplanar feature of the side chain played a critical role in modulating aggregation, (2) a noncovalent S–O interaction between the π-spacer and the donor unit ensured planarity between them during the formation of a high-quality polymer, and (3) the degree of torsion caused by substituted groups resulted in the polymer having a compact morphology due to its steric hindrance.[108–110] Therefore, the synthesized polymer named poly(BT-ThEDOT) exhibited a planer and porous structure to realize high EC performance with a green-and-blue color state. The porous microstructure morphology of the poly(BT-ThEDOT) film also contributed to enhancing the capacitance to 92 F g^{-1}, even at a 1.0 A g^{-1} current density, as shown in Fig. 4b. Coloration (blue to green) and bleaching (green to blue) indicate the corresponding EC color modulation for charging and discharging states with 46% optical color contrast.

PEDOT has already been extensively studied for supercapacitors due to its broad operational potential window, high conductivity, and stability, and its capacitance is found to be lower compared to that of known ordinary polymers, such as PANI and PPy.[111] The reason is the unavailability of a doping site and its large molecular weight. Therefore, introduction of 3,6-dialkoxythieno[3,2-*b*]thiophene in PEDOT–benzo[*c*][1,2,5]thiadiazole (BTD) renders an appropriate donor unit and forms a relatable D–A-type polymer for charge transportation. A p-doped poly[4,7-bis(3,6-dihexyloxy-thieno[3,2-*b*]thiophen-2-yl)]-benzo[*c*][1,2,5]thiadiazole (PBOTT)–BTD electrode was used to fabricate a symmetrical (polyethylene terephthalate [PET]/ITO/PBOTT–BTD//PBOTT–BTD/ITO/PET) and asymmetrical (PET/ITO/PEDOT//PBOTT–BTD/ITO/PET) flexible ECS device.[112] The asymmetrical ECS device achieved high energy density (5.7 W h kg^{-1}), power density (1.2 kW kg^{-1}), and capacitance (21 F g^{-1}) at an operating voltage of 1.4 V compared to the symmetrical ECS device. The device showed its charging-to-discharging color state as blue (0.6 V) to green (−0.4 V), and the change in color was due to the formation of poloron and bipoloron carriers. In addition, the reversibility and stability of the colored states during charging–discharging cycles indicated that the device was a smart ECS device. Several studies have explored D–A–D-type polymer-based devices to monitor the real-time energy storage level. A single-electrode system of EDOT (donor) and isoindigo (acceptor) shows a poor response for charge/discharge stability with a capacitance of 1.7 mF cm^{-2}.[113] A polymer film was analyzed by adding π-spacers in a D–A–D-type polymer to optimize the thin-film structure, which enhanced the
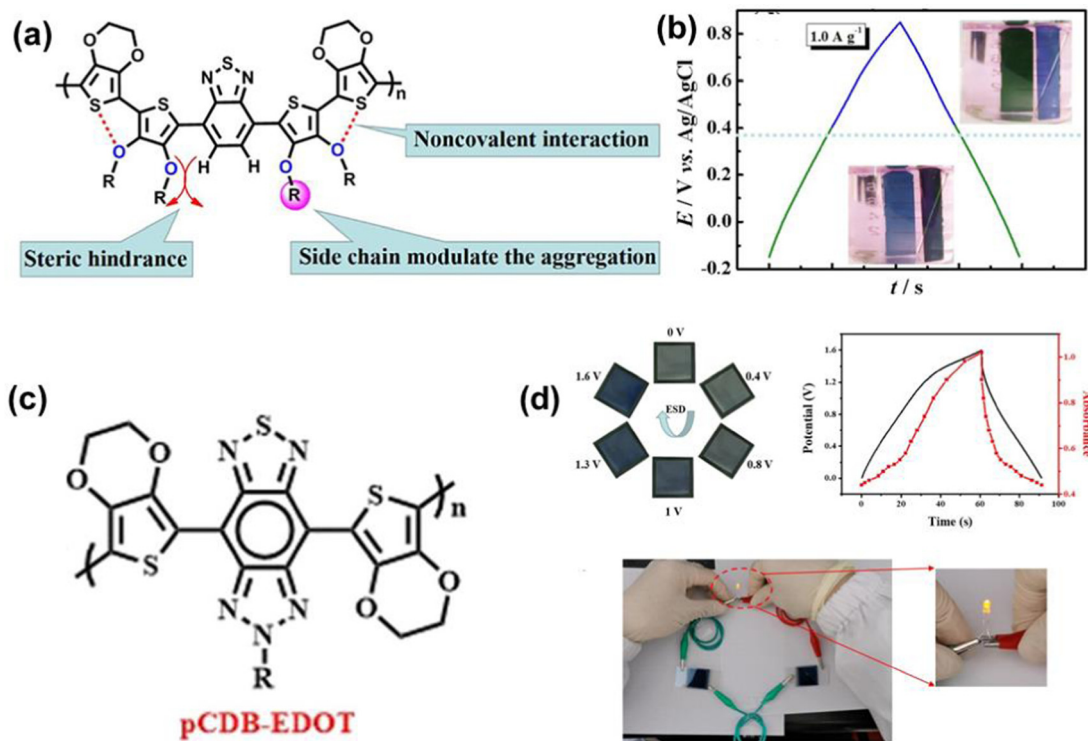

Fig. 4 Chemical structure of the D−π−A−π−D-type polymer (a) and the charging–discharging response of a film with color notation at 1.0 A g^{-1} (b). Adapted from ref. 55. Copyright [2020] Elsevier. Chemical structure of pCDB−EDOT (c) and ECS device of pCDB−EDOT//PEDOT with synchronized optical and GCD curves with a glowing LED (d). Reprinted from ref. 116. Copyright [2021] American Chemical Society.

capacitance compared to the respective independent polymer units. However, selective donor and acceptor units in a complete D–A–D-type polymer also decide the electronic and optical properties.[114,115]

This new strategy of D–A–D-type conjugated polymer synthesis with donor EDOT and acceptor chalcogen-diazolobenzo-triazole (CDB) units has been investigated.[116] A bulky planer structure of the CDB unit with a long alkyl chain at the N position usually exhibits a large steric hindrance with the EDOT unit and inhibits the formation of a dense membrane. Fig. 4c shows the polymer structure of synthesized pEDOT–CDB. A loosely stacked structure promotes fast ion transport and protects the film from damage under a repetitive redox process, leading to enhanced performance.[108] Therefore, a solid-state asymmetric ECS device was designed using pCDB–EDOT (positive electrode) and PEDOT (negative electrode) with a LiBF$_4$/[BMIM]BF$_4$ electrolyte in a two-electrode system. The combination of the ECS led to a fast coloration (1.19 s) and bleaching (0.98 s) response toward the dark-green and blue state of the device. The device showed different color intensities of dark green and blue depending on the applied voltage, as shown in Fig. 4d, which

shows a linear change for charging–discharging at a fixed current density. Charging–discharging and absorption of the device were simultaneously analyzed in accordance with the changing EC color intensity. The device showed a change from dark green to blue during the charging period and reverted to its natural color state on discharging, delivering a maximum energy density of 0.658 μW h cm^{-2} and a power density of 80.24 μW cm^{-2} at a current density of 0.1 mA cm^{-2}. This excellent output of the device has been depicted by a glowing light-emitting diode (LED), as shown in Fig. 4d. The pCDB–EDOT//PEDOT ECS was discharged through a yellow LED (1.8 V, 0.04 W), and the LED lit up for more than 60 s, showing a high discharge capacity characteristic of the D–A–D polymer unit.

In addition to designing a molecular structure, an efficient charge transfer process and low sheet resistance of the substrate equally enhance the ECS operation. Continuous use of ITO and FTO transparent electrodes, AgNWs, encapsulated graphene layers, and CNT-embedded structures also improves the charge transportation mechanism. However, AgNWs suffer from oxidation and corrosion, which lead to poor performance and stability.[117,118] Therefore, Cai et al. prepared an Ag grid PET
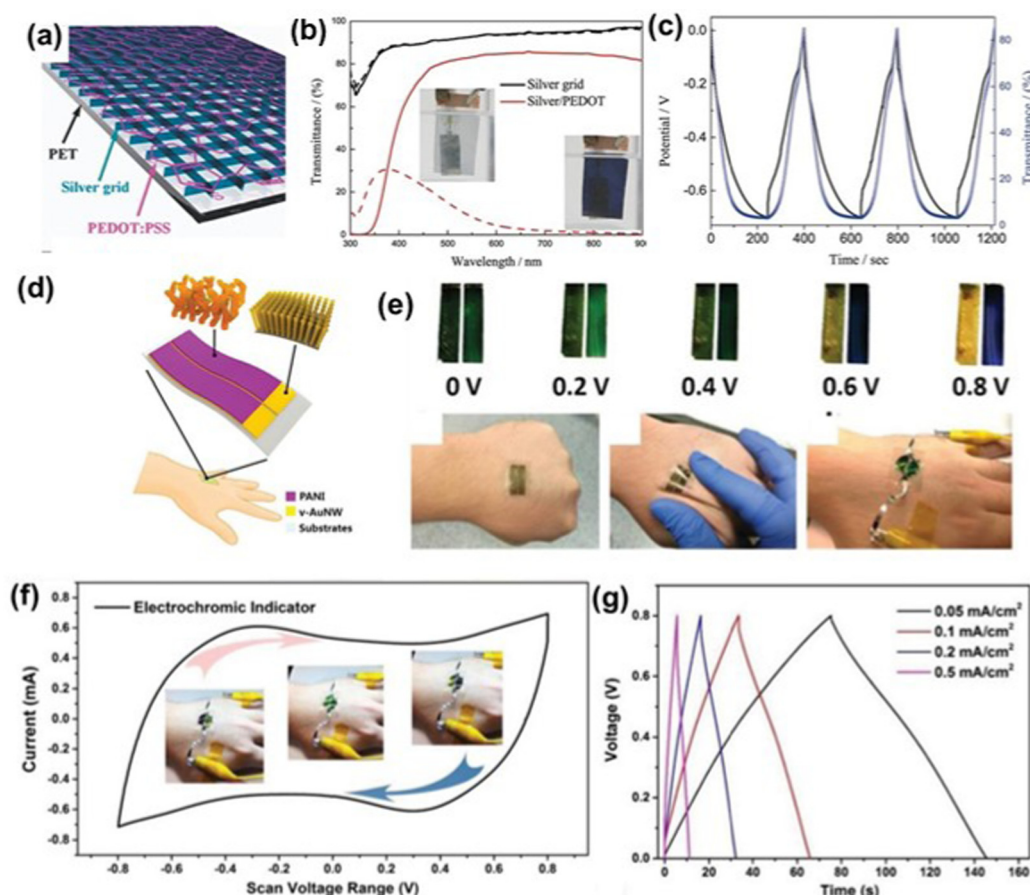

Fig. 5 Schematic illustration of an Ag grid/PET substrate with a PEDOT:PSS film (a). Transparent spectra of colored (−0.7 V) and bleached (0.1 V) state of WO$_3$@Ag and WO$_3$@Ag–PEDOT films (b). Synchronized GCD and transmittance spectra of WO$_3$@Ag-PEDOT films at 1 A g^{-1} (c). Reproduced from ref. 119. Copyright [2015] Wiley-VCH. Schematic illustration of a wearable v-AuNW/PANI device (d) with each photograph having a different color modulation at a different potential (e). CV performance (f) and GCD profile at different current densities of the device (g). Reprinted from ref. 122. Copyright [2018] Wiley-VCH.

substrate covered by PEDOT:PSS to create a hybrid film, as shown in Fig. 5a.[119] This conductive hybrid film over the PET substrate exhibited high transparency ($\sim 70\%$) with 0.62 Ω sq^{-1} sheet resistance. One additional advantage of a PEDOT:PSS layer is protection of the Ag grid from natural oxidation. This substrate was used for the electrodeposition of a WO$_3$ film. A significant difference was found between the colored and the bleached state in transmittance spectra, as shown in Fig. 5b, with and without the PEDOT:PSS structure of the WO$_3$-coated Ag grid. High optical modulation ($\sim 81.9\%$) at 633 nm was achieved by the WO$_3$/PEDOT/Ag/PET hybrid film. The charging–discharging process was due to the production of possible redox species of W^{6+} and W^{5+} at a current density of 1 A g^{-1}. Fig. 5c shows the instantaneous behavior of energy storage levels with a change in optical transmittance. The dark-blue color of the film indicates a fully charged state, and its reversal to a natural colorless state shows the discharging state. A complete reversible color state developed within the potential range of 0.0 to –0.7 V, with a capacitance of 221.1 F g^{-1} at a current density of 1 A g^{-1}.

Polymer-based supercapacitors have also been explored in wearable energy storage devices, skin-mountable electronics, and on-skin biomedical healthcare systems.[120,121] The impressible electrochemical features of such devices with multiple applications in wearable electronics at the same time have attracted much attention. An *et al.* successfully fabricated a wearable skin like ECS self-assembled with gold nanowires (v-AuNWs) and a PANI film over a PET substrate, as shown in Fig. 5d.[122] A AuNW film provides high stretchability, conductivity, and softness for retaining integrity under several deformations and provides a high surface area for PANI deposition.[123] This pattern can also be used for making tattoolike patches on soft human skin and for direct use in wearable devices. Symmetrical EC devices are designed by using fabricated PANI/AuNW electrodes, where two different color possibilities exist at one potential value. The positively charged electrode shows a deep-blue color, while the negatively charged electrode shows a yellow color. AuNW-based electrodes have also been designed for human skin to draw a tattoo electrode patch, as shown in Fig. 5e. Under a complete potential scan from −0.8 to 0.8 V, as shown in Fig. 5f, a reversible color-switching cyclic voltammetry (CV) pattern shows a quasi-reversible rectangular pattern with an aerial capacitance of 5.13 mF cm^{-2}, while a linear trend of the charging/discharging profile is observed under varying current densities, as shown in Fig. 5g, with simultaneous color-changing ability.

Moreover, CPs can be combined with carbonaceous materials for improving the overall device performance. Carbonaceous and nanostructured materials are widely applicable for designing commercial energy storage devices.[124] Jiao *et al.* recently fabricated an electrode using CNTs/Au/PPy/PET, which exhibits low charge transfer resistance and low equivalent series resistance compared to Au/PPy/PET and PPy/PET electrodes and therefore shows a high capacitance of 23.9 mF cm^{-2} at a current density of 0.5 mA cm^{-2}. Due to the formation of polorons at negative (−0.9 V) potential, visual identification of the electrode was noticeable, from black/brown color to yellow color, during charging.[125]

De-doping of anions at a negative voltage forms a neutral molecular chain, resulting in a strong absorption band corresponding to the yellow-green color. Therefore, to keep the same electrode characteristics, an asymmetric flexible ECS was designed by selecting a counter electrode MnO$_2$/PET (as a positive electrode) through a PDMS spacer filled with aqueous LiClO$_4$ solution. This asymmetric flexible ECS device showed color-to-color switching (blue to yellow) between 0 and 1.8 V, with a maximum areal energy density of 4.03 kW h cm^{-2} at a current density of 0.2 mA cm^{-2}.

Improving the working potential window to realize high energy density in practical applications is still a great challenge. Therefore, an attempt has been made to synthesize a multi-walled carbon nanotube-poly dibromo monomer and benzo-dithiophene compound (BDT75) (MWCNT–PBDTC) composite film.[127] In this synthesized material, MWCNTs work as an electron acceptor group and form a stable n-doped constituent polymer, which improves not only the polymer's conductivity but also mechanical strength. A symmetric supercapacitor was designed using a polyacrylamide (PAAM)-based electrolyte for MWCNT–PBDTC-based electrodes and provided a wide potential window of 4.8 V. A brown and gray color of the device was obtained in the uncharged and charged states, reflecting its high energy density of 174.7 W h kg^{-1}. A faster EC and energy storage function is governed by efficient electron transport between conductive MWCNTs and the polymer PBDTC. A few other works have also synthesized different conjugated polymers for exhibiting simultaneous ECS performance. Table 1 lists the polymers that have been investigated recently in the ECS field.

3.3 Inorganic material-based ECSs

Handling and fabrication of inorganic material-based ECS devices are much easier compared to others and improve surface-controlled application *via* nanomaterials. A self-supporting double-grid (DG) mesoporous V$_2$O$_5$ nanostructure-based electrode was designed for achieving enhanced pesudocapacitance.[130] The DG porous morphology provides high structural stability and a large active surface area, creating an accessible path for electrolyte ions.[131] A free-standing V$_2$O$_5$ network was fabricated by electrodeposition into a voided copolymer template network with a DG morphology. The surface morphology is shown in Fig. 6a with a scanning electron microscopy (SEM) image along with a symmetric design of a device filled with the lithium bis(trifluoromethylsulfonyl)imide (LiTFSI) electrolyte. Fast ion transportation was seen in the symmetric DG-V$_2$O$_5$ device in terms of the respective color change during the charging–discharging cycle. In Fig. 6aI, the letters "NO" and "KIA" correspond to the upper and bottom electrodes, respectively. The conversion from green-gray to a yellowish color is due to oxidation under charging conditions. Color modulation was observed in different colors (Fig. 6aII–III). Dynamic responses of optical behavior with a potentiometric measurement at a current density of 2.0 mA cm^{-2} are plotted together in Fig. 6b. A high color contrast and a high specific capacitance of 155 F g^{-1} were measured for this combination, which are governed by the extremely small pores of DG.

Table 1 Polymer-based ECS electrode/device assembly

Number	Polymer	ECS[a] device combination	Chromic modulation		ECS device performance		Ref.
			Charging	Discharging	Optical	Electrical	
1	Triphenylamine triazine/ditriaine (pTPATz and pTPADTz)	pTAPTz/LiBF$_4$//pEDOT[b]	Blue	Light green/red	—	—	126
2	CDB[c]–EDOT–CDB	pCDB–EDOT//PEDOT[d]	Blue	Dark green	ΔOD[e] $\approx$ 83%	4.65 mF cm^{-2}	116
3	MWCNT[f]–PBDTC[g]	MWCNT–PBDTC//LiClO$_4$/PC–PMMA[h]//MWCNT–PBDTC	Gray	Brown	—	174 W h kg^{-1} and 4.8 kW kg^{-1}	127
4	CNTs[i]/Au/PPy[j]/PET[k]	CNTs/Au/PPy/PET//MnO$_2$/ITO[l]/PET	Yellow green	Dark brown	—	4 μW h cm^{-2} at 0.2 mA cm^{-2}	125
5	Poly(4,7-bis(5-(2,3-dihydrothieno[3,4-b][1,4]dioxin-5-yl)-3,4-bis(hexyloxy)thiophen-2-yl)benzo[c][1,2,5]thiadiazol)	Electrode–poly(BT-ThEDOT)/ITO	Blue	Green	$\Delta T \approx$ 46%	92 F g^{-1} at 1 A g^{-1}	55
6	Ag/PEDOT:PSS	Electrode WO$_3$@Ag/PEDOT:PSS	Blue	Transparent	$\Delta OD \approx$ 81.9%	221.1 F g^{-1} at 1 A g^{-1}	119
7	QA[m] derivatives (C10QA–2T, C10QA–2EDOT, C10QA–2DT)	pC10QA–2EDOT//pC10QA–2EDOT	Blue	Yellow	$\Delta OD \approx$ 40%	322 F cm^{-3} at 5 A cm^{-3}	128
8	PBOTT[n]–BTD[o]	PBOTT–BTD//PEDOT	Blue	Green	—	3–6 W h kg^{-1} & 0.6–8 kW kg^{-1}	112
9	AuNWs[p]/PANI[q]	Symmetric AuNWs/PANI	Blue	Green	—	11.7 mF cm^{-2} at 10 mV s^{-1}	122
10	Triphenylamine-triazine-based conjugated microporous polymer	Two-pTTPATA polymer electrode	Red	Light yellow	—	81 mA h g^{-1}	104
11	Thiophene-based polythiophene derivative (pPHBT)	Single pPHBT electrode	Green	Yellow	—	96.7 mA h g^{-1}	129

[a] ECS: electrochromic supercapacitor. [b] EDOT: 3,4-ethylenedioxythiophene. [c] CDB: chalcogena-diazolobenzotriazole. [d] PEDOT: poly(3,4(ethylenedioxy)-thiophene). [e] OD: optical density. [f] MWCNT: multiwalled carbon nanotube. [g] PBDTC: poly dibromo monomer and benzodithiophene compound (BDT75). [h] PMMA: polymethylmethacrylate. [i] CNT: carbon nanotube. [j] PPy: polypyrrole. [k] PET: polyethylene terephthalate. [l] ITO: indium tin oxide. [m] QA: quaternized. [n] PBOTT: poly[4,7-bis(3,6-dihexyloxy-thieno[3,2-b]thiophen-2-yl)]. [o] BTD: benzo[c][1,2,5]thiadiazole. [p] AuNW: gold nanowire. [q] PANI: polyaniline.

Tae et al. manufactured a high-performance WO$_3$-based ECS that displayed the real-time capacity in dual functions.[132] A single-layer WO$_3$-coated ITO electrode was used with ferrocene (counterion), hydroquinone (HQ,) and Li$^+$-doped [EMI][TFSI] ion gel. A selective combination made the device transparent in the bleached state and display excellent performance. A noticeable difference in color contrast during charging–discharging was achieved (Fig. 6c and d), yielding 91% optical contrast with an aerial capacitance of 13.6 mF cm^{-2}. A selective process to design a WO$_3$-based ECS with an ion gel electrolyte was explored for utilization in wearable devices and it was shown that it can operate under high-temperature conditions. Nearly 64% higher capacitance was achieved at 40 °C compared to 0 °C due to the higher diffusion of ions at the same current density. Such dual-function ECSs are a real need for future technologies and for practical applications.

Shen et al. synthesized a novel flexible ECS based on AgNWs and WO$_3$ over a PDMS/PET substrate. Ultralong AgNWs (>200 μm) provided excellent interconnectivity to WO$_3$, with high conductivity and improved mechanical strength.[133] A strong conductive interaction between WO$_3$ and AgNWs led to improved insertion/extraction of ions, enhancing their EC performance. The combination of AgNWs–WO$_3$ electrodes displayed high ECS performance in a linear pattern of charging–discharging, with a CE of 80.2 cm^2 C^{-1} and a gravimetric capacitance of 138.2 F g^{-1}. To make better contact between the metal and inorganic EC oxide, a new and unique strategy was investigated by Kim et al. to form a nanofilament array (NFA)-embedded WO$_3$ film.[134]

An amorphous WO$_3$ film was initially deposited using radio-frequency (RF) magnetron sputtering, followed by electroforming treatment with Au tips, to create an NFA-embedded structure, as shown in Fig. 6e. Due to the formation of NFA, the insulating WO$_3$ film exhibited reversible bistable resistance between high and low resistance states. This resistive switching mechanism is explained by the reversible redox reaction at the electrode–electrolyte interface, and a low resistance state leads to accessible charge transfer dynamics.[135,136] This can be understood during the CV scan, where an NFA–WO$_3$-based electrode showed a large area compared to the pristine WO$_3$ electrode. NFA provides a conducting path for electron transport during long-term stability. This mechanism also induces a negatively charged oxygen ion in NFA regions, which is highly responsive to absorbed Li$^+$ at the electrode–electrolyte interface and, thus, responds to a fast redox reaction. Only WO$_3$ is an electrochromically active material in this system; therefore, it shows a change in the intensity of blue color in pristine WO$_3$ and an NFA-embedded WO$_3$ system, as shown in Fig. 6f. A significant optical contrast between them (NFA–WO$_3$ ~67%, pristine WO$_3$ ~ 55%, Fig. 6g and h) was measured with a change of 12%. Due to the same operating mechanism, the specific capacitance of WO$_3$ and NFA–WO$_3$ electrodes was measured as 133 and 214 F g^{-1} at a current density of 0.25 mA cm^{-2}, respectively (Fig. 6I and j). Thus, enhanced conductivity, higher electrochemical active surface area, and fast charge kinetics in an NFA-embedded WO$_3$ structure facilitate the design of a high-performance ECS.

Inorganic WO$_3$ is known for only a one-fold EC characteristic from transparent to blue color, and it is little difficult to
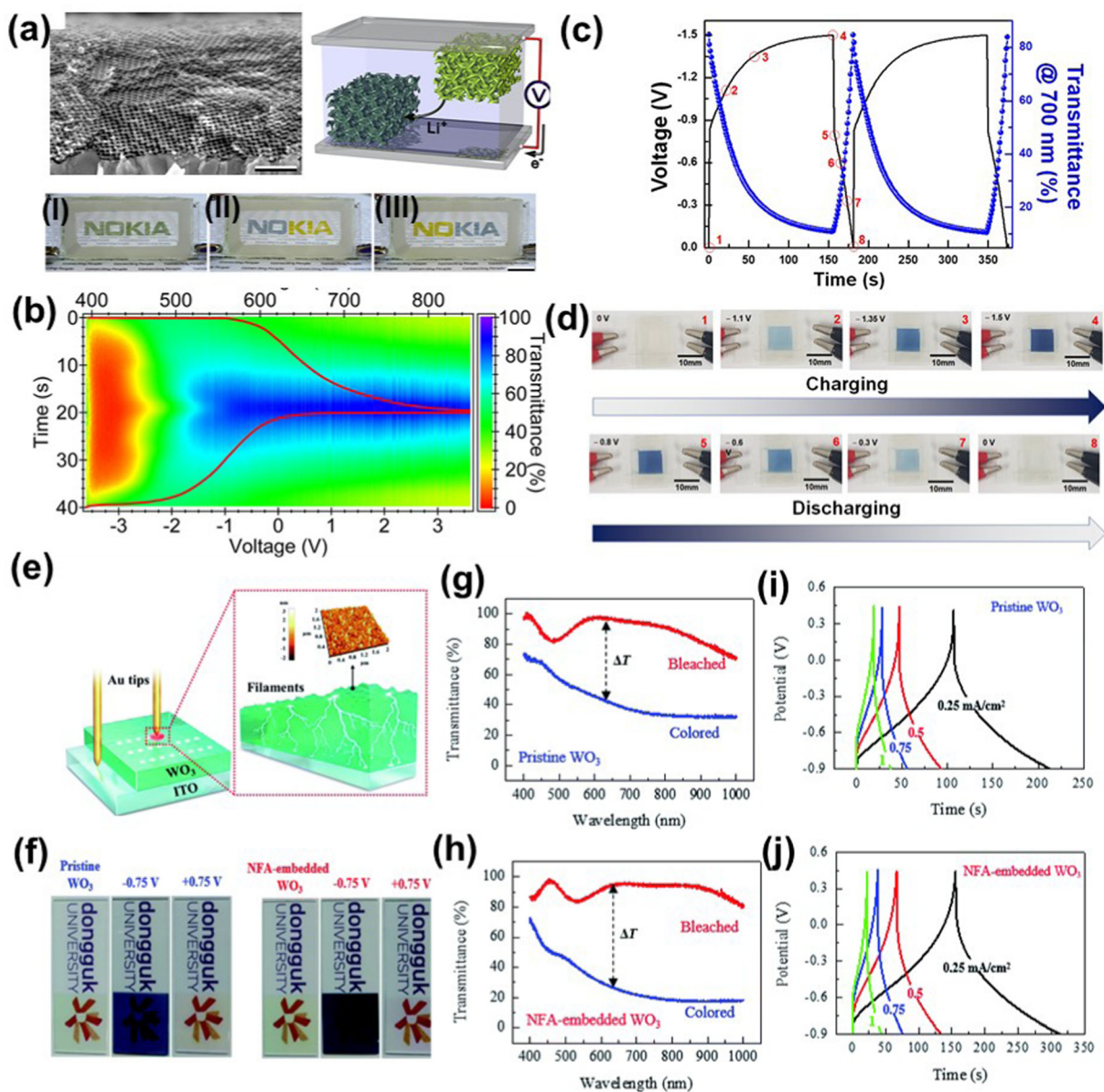
Fig. 6 SEM image of mesoporous V_2O_5 double-gyroid structure (aI), device structure of symmetric electrodes (aII), and different optical images with "NO" and "KIA" (aIII). Transmittance variation during chronopotentiometry with alternating current polarity (± 2 mA cm^{-2}) (b), Reproduced from ref. 130. Copyright [2012] American Chemical Society. GCD profile of a WO_3-based ECS at a current density of 0.4 mA cm^{-2} within a potential range of 0 to -1.5 V with *in situ* transmittance spectra (c), and photographs of the device during charging–discharging (d). Reproduced from ref. 132. Copyright [2018] American Chemical Society. Schematic drawing of the electroforming process for a conducting NFA across a WO_3 electrode film (e) and EC behavior of pristine WO_3 and NFA–WO_3 electrodes (f). Respective transmittance spectra for colored and bleached states (g and h) and their GCD profiles with different current densities (i and j). Adapted from ref. 134. Copyright [2020] The Royal Society of Chemistry.

examine the exact energy storage level in real-time charging and discharging. The dark-blue color indicates serious loss. The varying intensity between the transparent and the dark-blue color was qualitatively analyzed for leveling their intermediate energy levels. An aesthetic design using Fabry–Pérot (F–P) cavity-type WO_3 was investigated to observe multistep colors in ECSs.[137] A thin layer (100 nm) of metallic tungsten was placed between ITO and WO_3 layers, which cause the multiple interference resonance with peaks and valleys in a wavelength range from 380 to 780 nm. The F–P cavity absorbed some light and

reflected another wavelength of light on the electrode surface. This optical mechanism can be tuned for other colors (or wavelengths) by changing the WO_3 layer thickness.

A prototype solid-state flexible ECS device was fabricated with a thin planer architecture of two F–P cavities and was filled with a polyvinyl alcohol (PVA)/H_2SO_4 gel electrolyte, as shown in Fig. 7a. The green-colored (at 0% charging) supercapacitor showed different other colors corresponding to the charging percentage (Fig. 7b) and also showed a clear differentiation between these individual-colored states. The F–P cavity-type
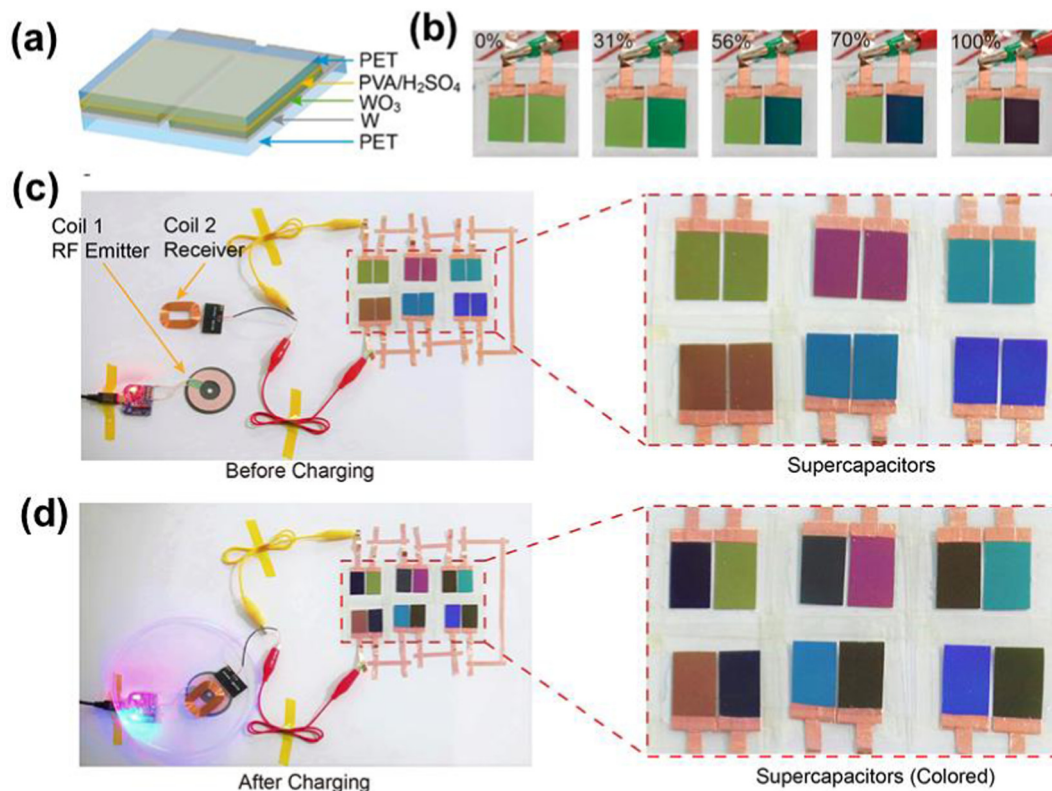
Fig. 7 Full-device fabrication of a Fabry–Pérot cavity-type ECS (a) with different color patterns (b). Wireless mechanism of connected devices before charging (c) and after charging (d). Reproduced from ref. 137. Copyright [2020] American Chemical Society.

ECS was also successfully designed for charging through a wireless power source. A series combination of six F–P ECSs with different color states were connected to a receiver antenna, as shown in Fig. 7c, showing their initial color states before charging. An RF emitter transmitted a frequency of 100 kHz for 15 s, which was received by the ECS receiver, as shown in Fig. 7d, which quickly charged from 0 to 3.6 V, reflecting its diverse color states. The charge states were also examined in terms of efficient power delivery by connecting to one or more LEDs. This new finding with regard to WO_3 suggests an intelligent, smart multicolored ECS device.

In addition to fabricating a single-layer electrochromically active WO_3 film for ECSs, recently, there has been some research on a NiO (anodic) film in combination with a WO_3 (cathodic) film. The combination of such dissimilar counter-electrochromically active materials often provides an avenue for faster charge transportation at each potential irrespective of the polarity. The redox behavior of both materials accelerates the charge transportation at the electrode–electrolyte interface. Therefore, two different ECSs with separate modifications of NiO- and WO_3-based electrodes were designed by one research group.

In the first approach, a mesoporous WO_3 film having small pores (20–50 nm) was synthesized for realizing the ultrafast response of device performance. A mesoporous structure leads to higher diffusivity for Li^+. Fig. 8a shows the synthesis of mesoporous WO_3 *via* the evaporation-induced self-assembly (EISA)-based sol–gel technique, followed by oxygen plasma

treatment to eliminate amorphous carbon.[138] The porous structure can easily be visualized by SEM, as shown in Fig. 8b. The prepared electrode was used to fabricate an ECS device having an ion storage counter-NiO electrode along with an electrolyte containing $LiClO_4$ in propylene carbonate, as shown in Fig. 8c. As a negative voltage was applied to the WO_3 electrode, reduced (W^{5+}) and oxidized (Ni^{3+}) species were formed at their respective electrode surface. The redox state turned the device blue. The reverse voltage at the electrodes triggers a reverse redox reaction, and the device appears transparent as a result. Fast dynamic response of Li^+ insertion/extraction at the mesoporous electrode surface indicated fast device performance. The simultaneous capacitive and EC performance is shown in Fig. 8d at a current density of 1 mA cm^{-2}. Transmittance decreased once the device was charged and it displayed a blue color at −2.3 V, where the ECS was fully charged. At the same load current, a symmetrical GCD pattern was seen and no significant degradation in optical contrast was observed from the initial transparent color. This is due to fast and effective ion transport by the mesoporous WO_3 electrode compared to the compact WO_3 film, as shown schematically in Fig. 8e and f.

The second effective approach to obtaining a high-performance ECS was to keep the same compact WO_3 structure while improving the conductivity of the opposite NiO electrode.[139] The same group explored this device configuration by varying the Cu metal dopant NiO film, as shown in Fig. 8g. A Li^+ containing polyionic gel electrolyte was sandwiched between
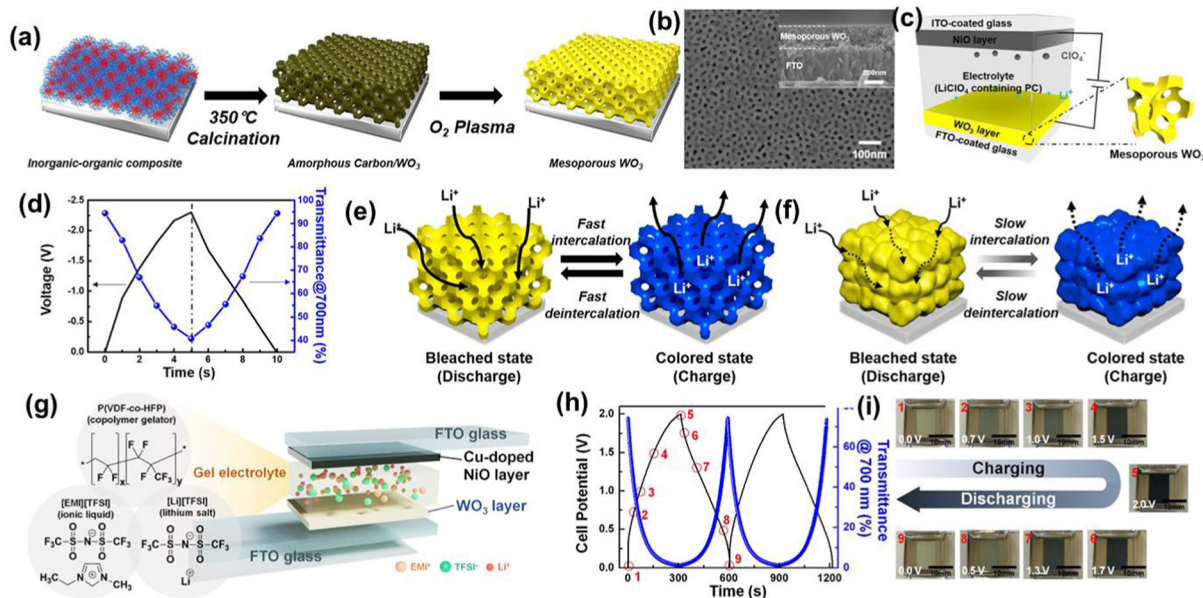
Fig. 8 Methodology of the preparation of mesoporous WO$_3$ (a) and its SEM image (b). NiO/WO$_3$ two-electrode device (c). Synchronized GCD and transmission spectra of the device at constant current density (d). Functioning Li$^+$ intercalation during charging–discharging operation for mesoporous (e) and nonmesoporous (f) WO$_3$ electrodes. Reproduced from ref. 138. Copyright [2020] Nature (Open access). ECS device design of the Cu-doped NiO/WO$_3$ based electrode and gel electrolyte (g) and the GCD profile of the device with changing optical spectra (h). Real optical photograph of the device during charging–discharging (i). Permission from ref. 139. Copyright [2020] American Chemical Society.

two electrochromically active electrodes, and 7% Cu doped NiO with a 7× spin-coated film was characterized for high conductivity and used for ECS device fabrication. The ECS appeared dark blue upon charging and becomes completely transparent upon discharging (Fig. 8h and i). Faster diffusion of Li$^+$ was triggered by the highly conductive metal-doped NiO electrode and provided 85% optical contrast with 14.9 mF cm^{-2} areal capacitance. Successful operation of this combination in a wide temperature range from 0 °C to 80 °C is of high practical use. Similarly, to achieve superior overall ECS performance, MOF-derived NiO electrodes were prepared. The film not only had a highly porous structure and large surface area but also provided strong binding to the ITO substrate.[142] Other studies have discovered inorganic materials for ECSs in the past few years, which are summarized in Table 2 with their device combinations and performance.

3.4 Hybrid and composite-based ECSs

This section consists of hybrid and composite-based ECSs to describe their importance to improve overall efficiency and performance. A hybrid device was designed by Zhu et al. using WO$_3$, MnO$_2$, and Ppy electrodes.[145] Two different WO$_3$–MnO$_2$ and WO$_3$–Ppy hybrid ECSs were integrated using the process defined in Fig. 9a. Two FTO electrodes coated with WO$_3$ and MnO$_2$ (or Ppy) were joined by a copper wire to build a hybrid solid-state device in parallel geometry. Enhanced capacitance was obtained after adding Ppy and MnO$_2$, as seen from the enlarged CV-encircled area in Fig. 9b, and the capacitance was 11.38 and 14.21 mF cm^{-2} at a 20 mV s^{-1} scan rate, respectively. A more obvious high specific capacitance of 45 mF cm^{-2} at a current density of 1 mA cm^{-2} was measured for WO$_3$–MnO$_2$ from GCD curves (Fig. 9c) compared to pure WO$_3$. A clear,

distinguishable color of the device during the different charging stages for both hybrid combinations (Fig. 9d and e) and, therefore, accurate and quantifiable measurements of the electrical energy storage capacitor could be estimated from the normalized optical density (OD) of the ECS and determined by the calibration curves.

Similarly, metal oxides with CPs (e.g., PEDOT/WO$_3$, PANI/TiO$_2$, poly(3,4-ethylenedioxypyrrole)–Au–WO$_3$, poly(indole-6-carboxylic acid)/TiO$_2$) have been widely studied for multi-color-state and high supercapacitive properties.[146–148] Improving charge transport by increasing the overall conductivity is a salient feature behind the synthesis of these composite materials. Recently, polyindole-based CPs have been studied because of their high electrical and thermal stability.[149–151] An effective strategy to synthesize a composite structure of p-doped polyindoles and n-doped WO$_3$ improves the EC conversion rate in the combined system.[152]

Guo et al. successfully synthesized a nanocomposite structure of poly(5-formylindole)–WO$_3$ and combined it with a PEDOT-based electrode to prepare an asymmetric ECS. Three-stage electrochromism was displayed by the poly(5-formylindole)–WO$_3$-based electrode with dark green, yellow, and yellow green with a high CE, high optical contrast, and a high areal specific capacitance of 34.1 mF cm^{-2} in an electrochemical cell.[150] In a device assembly, PEDOT serves as a negative redox-active electrode and helps improve linearity in the GCD curve. The combination also possesses a low IR drop, which indicates high electron transfer efficiency and low equivalent series resistance. Under charging conditions, the device converts its yellow color to blue-black and reverts to yellow upon discharging and reflects nearly 61% change in transmittance with 10.38 mF cm^{-2} specific capacitance. The same researchers explored two other hybrid

Table 2 Inorganic material-based ECS electrode and solid-state device

Number	ECS[a] device combination	Chromic modulation		ECS device performance		Ref.
		Charging	Discharging	Optical	Electrical	
1	PET[b]/W-WO$_3$/PVA[c]/H$_2$SO$_4$/PET	Green, blue-green, sapphire blue, and dark violet	Green, blue-green, sapphire blue, and dark violet	10–108 cm^2 C^{-1}	68.4 mF cm^{-2} at 0.2 mA cm^{-2}	137
2	AgNWs[d]/WO$_3$@PDMS[e]	Blue	Transparent	80 cm^2 C^{-1}	138.2 F g^{-1}	133
3	WO$_3$/Li$^+$-HQ[f]	Blue	Transparent	61.9 cm^2 C^{-1} ($\sim$91%)	13.6 mF cm^{-2} at 0.4 mA cm^{-2}	132
4	FTO[g]/LMO[h]/Ta$_2$O$_5$/LiNbO$_3$/Ta$_2$O$_5$/WO$_3$/FTO	Dark blue	Light green	$\sim$95.8 cm^2 C^{-1}	16.2 W cm^{-3} 0.2 W h cm^{-3}	140
5	NFA[i]-embedded WO$_3$	Blue	Transparent	128 cm^2 C^{-1}	214 F g^{-1}	134
6	Cu-doped NiO/WO$_3$	Dark color	Transparent	$\Delta T \approx 85\%$	14.9 mF cm^{-2} at 0.1 mA cm^{-2}	139
7	NiO–CO$_5$//Fe$_2$O$_3$	Dark brown	Yellow	—	0.8 mF cm^{-2} at 0.4 mA cm^{-2}	141
8	MOF[j]-NiO/ITO[k]	Dark black	Transparent	41.08%	2.08 F cm^{-2} at 1 mA cm^{-2}	142
9	h-WO$_3$ BNW[l]/FTO	Dark blue	Transparent	$\Delta T \approx 45.81\%$	22.7 mF cm^{-2}	143
10	NiO/V$_2$O$_5$/rGO[m]//MrGO	Orange	Dark green	—	34.0 W h kg^{-1} 1022 W kg^{-1} at 2.0 A g^{-1}	144
11	Mesoporous WO$_3$/NiO	Dark	Transparent	$\Delta T \approx 76\%$	2.57 mF cm^{-2}	138
12	Symmetric DG[n]–V$_2$O$_5$	Yellow	Green/gray	—	155 F g^{-1}	130

[a] ECS: electrochromic supercapacitor. [b] PET: polyethylene terephthalate. [c] PVA: polyvinyl alcohol. [d] AgNW: silver nanowire. [e] PDMS: poly(dimethylsiloxane). [f] HQ: hydroquinone. [g] FTO: fluorine doped tin oxide. [h] LMO: LiMn$_2$O$_4$. [i] NFA: nanofilament array. [j] MOF: metal oxide framework. [k] ITO: indium doped tin oxide. [l] BNW: branched nanowire arrays. [m] rGO: reduced graphene oxide. [n] DG: double-gyroid.

combinations, poly(indole-6-carboxylic acid) (P6ICA)–TiO$_2$ and (P6ICA)–WO$_3$, with three EC color states (yellow, green, and brown, and dark green, yellow, and yellow-green), respectively.[146,149] An asymmetric ECS device was created by

Fig. 9 Fabrication of a WO$_3$-based hybrid ECS and the equivalent circuit (a). CV curves of the device with pure WO$_3$ at a 20 mV s^{-1} scan rate (b) and its respective GCD profile (c). EC effect of WO$_3$–Ppy and WO$_3$–MnO$_2$ hybrid supercapacitors (d and e). Reproduced from ref. 145. Copyright [2015] The Royal Society of Chemistry.

combining anodic electrode and cathodic PEDOT. In the P6ICA/TiO$_2$//PEDOT combination, the areal capacitance was 9.65 mF cm^{-2}, with a charging status noticeable by a light-green–dark-blue color conversion, although yellow–green conversion was obtained during discharging in the P6ICA–WO$_3$//PEDOT device, reflecting 16.69 mF cm^{-2} areal capacitance.

Two-dimensional materials have been successfully established for their high electrical conductivity and are used in a vast array of fields, including electrochemistry and optoelectronics.[153,154] Recently, 2D transition metal carbides (MXenes) have been explored in the ECS system. MXenes were primarily used for manufacturing high-performance supercapacitors, but their color-changing behavior was unexplored.[155,156] Recently, Li et al. developed MXene–PEDOT heterostructures using electrochemical deposition. Penetration of the EDOT monomer into the layer of MXene flakes is beneficial for fast ion transportation.[157]

Very recently, Sanjoy et al. have applied two-dimensional CONASH thin films for energy storage devices. Changing the redox property of Fe(II)/Fe(III) in polyFe-2D nanosheets is governed by the anisotropic charge transfer between the in-plane and the internanosheets, leading to improved charge storage performance.[158] The high density of Fe(II) ions in the dense hexagonal structure of polyFe-2D leads to a high volumetric energy density of 13.8 mW h cm^{-3}. Changing the redox state of Fe (II)/Fe(III) results in the red to colorless EC state of the CONASH electrode where the pure colorless state appears due to the poor π-conjugation in the tritopic bidentate ligands.[159] The same research group has also explored for the first time the supercapacitive behavior of metallo-supramolecular polymer (MSP) thin films. The designed structure of the Fe(II) and Ru(II) based MSP delivers a high volumetric capacitance of 62.6 F cm^{-3} and 98.5 F cm^{-3} and its combination as an asymmetric device with anodic PB delivers a higher energy density compared to the Li-ion thin film batteries.[160]

Varying the core structures in Fe^{2+} containing EC metallo-polymers also results in a ligand modulated capacitive behavior and can be taken to tune the EC color states.[85] A two-electrode
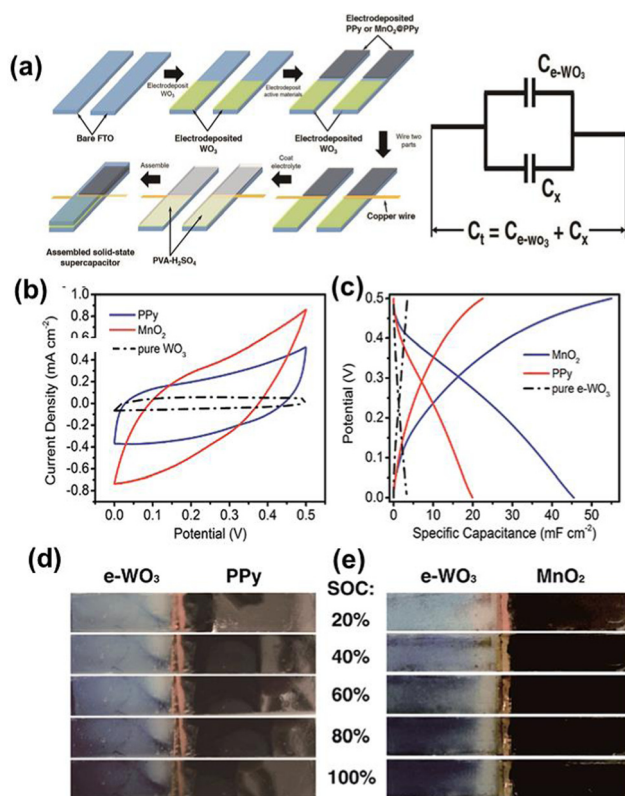
configured symmetric EC metallopolymer supercapacitor (poly-Fe-L2) was shown to deliver a high volumetric capacitance of 544.6 F cm^{-3} (compared to poly-Fe-L1 and poly-Fe-L3) at 1.0 A g^{-1} current density with color (orange) to color (green) transition. Variation in the ligand structures affected the charge storing property by changing the electrical conductivity and porosity. The extended conjugation in ligand L2, superior to L1 and L3, enhanced plane conductivity and improved the charge delocalization pathway via π–π interlayer interaction. The high conductivity of the metallopolymer offers higher ionic mobility and hence a plausible redox hopping mechanism around the Fe^{2+} center.

However, the ongoing challenges of the fabrication of large-area materials with controlled homogeneous microstructure and interface properties and dealing with high fabrication cost have been resolved by Guofa et al. by synthesizing a Fe(II)-based metallo-supramolecular polymer film by using electrostatic spray deposition techniques.[161] The film exhibits both EC and energy storage functions, showing a change from a violet color to transparent during the charging process with 73.6% optical contrast and delivering 18.24 mA h g^{-1} gravimetric capacity at 0.5 A g^{-1} current density. In addition to this material, metallo-organic assemblies were reported by Ofir et al., with layered composites of MWCNTs and PEDOT:PSS, operating under low potential (−0.6 V to 2 V) and displaying high energy (2.2 W h kg^{-1}) and power (2529 W kg^{-1}) density.[162] The simultaneous functioning of the metallo-organic layer is linked to the chromic modulation via the storage of holes which also promotes a high coloration efficiency (99%) and a fast switching time (2 s). A few recent studies on the dual role of these materials are presented in Table 3.

Fig. 10a shows a real photograph of the prepared electrode corresponding to a Ti$_3$C$_2$T$_x$ (up) and PEDOT/Ti$_3$C$_2$T$_x$ (down) thin film. Since MXene has high electrical conductivity compared to PEDOT, MXene also works as a current-collecting layer and PEDOT as a charge storage layer. A fast doping de-doping process occurs during redox reactions at the surface and gives a rectangular CV curve, even at a high scan rate (1000 mV s^{-1}), as shown in Fig. 10b, which is much closer to an ideal capacitor. The GCD curve also reflects a linear relationship between changing potential and time with different current densities (Fig. 10c). Fivefold higher areal capacitance (2.4 mF cm^{-2} at 10 mV s^{-1}) was measured in this hybrid combination compared to the pristine MXene microsupercapacitor.[157] Moreover, the deep blue to colorless transition was found in the voltage range from −0.6 to 0.6 V. A large operation potential window allows for high energy-storing capability and delivers up to 8.7 mW h cm^{-3} specific volumetric energy density at 0.55 W cm^{-3} power density, as summarized in the Ragone plot (Fig. 10d). Some studies have also worked on the MXene–EC material system but have focused on only energy storage properties rather than defining the ECS system. Thus, there are still several possible avenues to synthesize a hybrid network with MXene structure for an efficient ECS system.

Due to the ever-increasing demand for microsize supercapacitors (MSCs), stimulus-responsive microsize supercapacitors

Table 3 Hybrid and composite-based solid-state ECS[a]

Number	ECS[a] device combination	Optical response		ECS performance		Ref.
		Charging	Discharging	Optical	Electrical	
1	EG[b]/V$_2$O$_5$–MSC[c]	Purple	Colorless	—	20 mW h cm^{-3} and 235 W cm^{-3} at 10 mV s^{-1}	163
2	P6ICA[d]–WO$_3$//PEDOT[e]	Blue-black	Yellow-green	763 cm^2 C^{-1}	13.69 mF cm^2	149
3	PEDOT/Ti$_3$C$_2$T$_x$ (MXene)	Deep blue	Colorless state	—	2.4 mF cm^2 at 10 mV s^{-11}	157
4	P6ICA–TiO$_2$//PEDOT	Dark blue	Light green	—	9.65 mF cm^{-2}	146
5	e-WO$_3$//Ppy[f] (//MnO$_2$)	Dark	White	—	11.38 mF cm^{-2} at 20 mV s^{-1}	145
6	Au/Ag core–shell–WO$_3$ nanotube–PDMS[g]/ PEDOT:PSS[h]-(PAAM[i])–hydrogel electrolyte	Blue	Transparent	83.9 cm^2 C^{-1}	471.0 F g^{-1}	167
7	WO$_3$//Prussian white	Blue	Transparent	$\Delta T \sim 53.6\%$	1.97 mF cm^{-2} at 0.1 mA cm^{-2}	168
8	Poly(5-formylindole) (P5Fin)/WO$_3$//PEDOT	Blue-black	Yellow	627 cm^2 C^{-1}	10.38 mF cm^{-2}	150
9	AgNW[j]/Ni(OH)$_2$–PEIE[k]/PEDOT:PSS	Deep blue	Transparent	517 cm^2 C^{-1}	443 F cm^{-3}	169
10	AgNWs/rGO[l]/WO$_3$	Dark	Transparent	64.8 cm^2 C^{-1}	47.8 W h kg^{-1} and 16.9 kW kg^{-1}	170
11	Triphenylamine/dithienothiophene	Blue	Orange	$\Delta T \sim 60\%$	43 W h K g^{-1} at 10 A g^{-1}	171
12	BT[m]/PANI[n]	Light green/ dark blue	Light gray/ light blue	60 cm^2 C^{-1}	340 F g^{-1} at 1 A g^{-1}	172
13	LMO[o]@LNO[p]/WO$_3$	Dark blue	Light yellow	$\Delta T \sim 42.1\%$	106.1 W h kg^{-1} and 574.7 W kg^{-1}	173
14	GO[q]/PANI[r]	Yellow	Dark blue	41 cm^2 C^{-1}	137 mF cm^{-2} at 5 mV s^{-1}	174
15	MnO$_2$/V$_2$O$_5$/rGO[l]//MrGO[s]	Green	Orange	263.1 cm^2 C^{-1}	1403 F g^{-1} at 5 mV s^{-1}	175
16	G-CuS[t]/PANI[r]	Light green	Dark green	40%	17.3 mF cm^{-2} at 0.025 mA cm^{-2}	176
17	HbG[u]/PANI[r]	Light green	Dark green	60%	598 F g^{-1} at 1.0 A g^{-1}	177
18	Co(II)/Os(II)/Fe(II)/M(L)$_2$[v]//TiO$_2$	Dark yellow	Pale yellow	—	2.2 F g^{-1} at 0.06 mA cm^{-2}	178
19	Metallo supramolecular (poly Fe)	Blue	Transparent	750.3 cm^2 C^{-1}	18.24 mA h g^{-1} at 0.75 A g^{-1}	161
20	Poly Fe-2D/FeHCF[w]	Colorless	Red	—	83.8 F cm^{-3} at 1 A cm^{-3}	158

[a] ECS: electrochromic supercapacitor. [b] EG: exploited graphene. [c] MSC: microsize supercapacitor. [d] P6ICA: poly(indole-6-carboxylic acid). [e] PEDOT: poly(3,4-ethylenedioxy thiophene). [f] Ppy: polypyrrole. [g] PDMS: poly(dimethylsiloxane). [h] PSS: polystyrene sulfonate. [i] PAAM: polyacrylamide. [j] AgNW: silver nanowire. [k] PEIE: polyethylenimine ethoxylated. [l] rGO: reduced graphene oxide. [m] BT: benzo[c][1,2,5]thiadiazole. [n] PANI: polyaniline. [o] LMO: LiMn$_2$O$_4$. [p] LNO: LiNbO$_3$. [q] GO: graphene oxide. [r] PANI: polyaniline. [s] MrGO: metal-reduced graphene oxide. [t] G-CuS: graphene-copper sulphate. [u] HbG: hydrogen bonded graphene. [v] M(L): metal–ligand. [w] FeHCF: Fe-hexacyanoferrate.
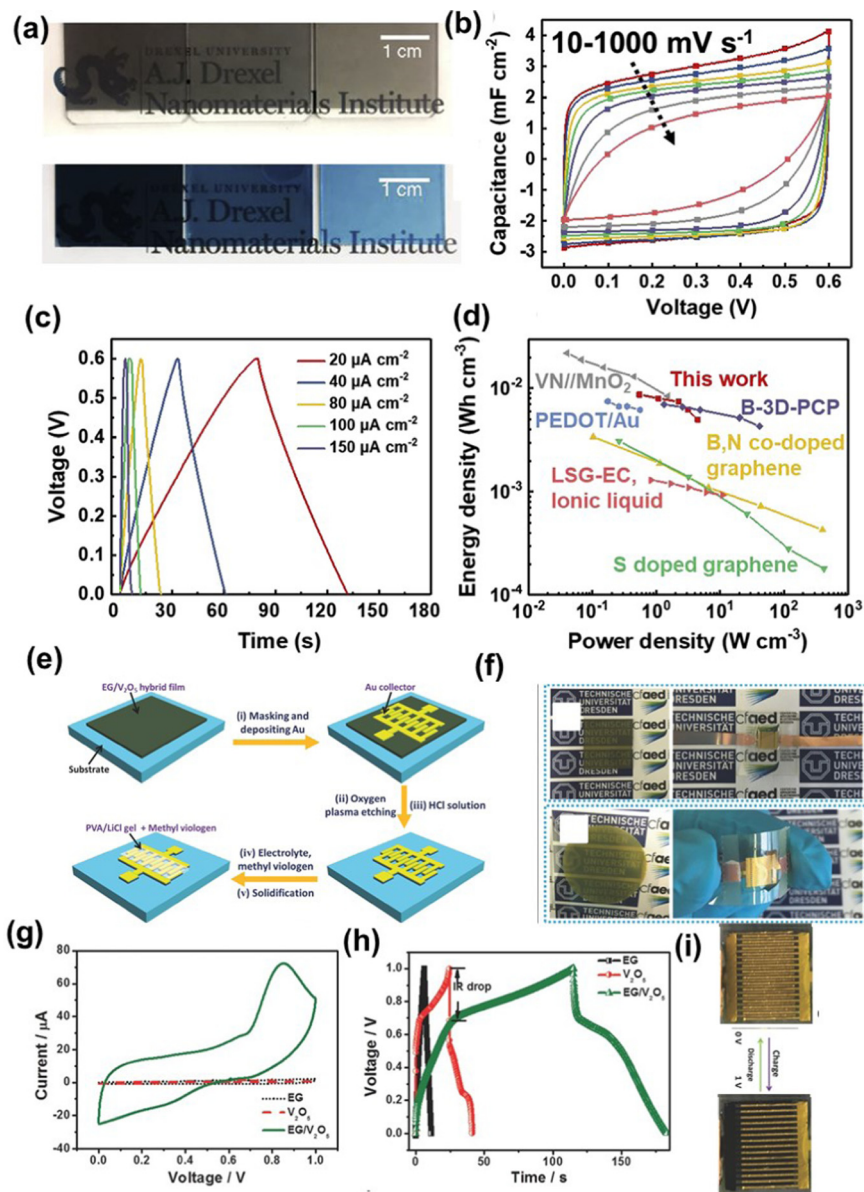
Fig. 10 Digital photographs of $Ti_3C_2T_x$ (up) and $PEDOT/Ti_3C_2T_x$ (down) thin films (a). CV (b) and GCD (c) measurement of $PEDOT/Ti_3C_2T_x$ with a different scant rate and current density, respectively. Ragone plot showing the superior energy and power density of a $PEDOT/Ti_3C_2T_x$ ECS compared to other reports (d). Reproduced from ref. 157. Copyright [2019] Elsevier. Step-wise fabrication of the SR-MSC hybrid electrode (e) and a real photograph of the device with glass and PET substrate (f), and CV performance (g) and GCD (h) profile in a 0 to 1 V potential window. EC color images of stimulus-responsive microsize supercapacitors during charging and discharging (i). Reproduced from ref. 163. Copyright [2016] Wiley-VCH.

(SR-MSCs) having a reversible EC window were developed. Two-dimensional exploited graphene (EG)–V_2O_5 hybrid nanopaper was designed (stepwise methodology is shown in Fig. 10e) for delivering high volumetric capacitance.[163] A real image of EG–V_2O_5 and the MSC device is shown in Fig. 10f with glass and a PET-supported substrate. Enhanced areal capacitance was noted for the EG–V_2O_5 device, as seen from the enlarged area of the CV curve (Fig. 10g), compared to EG and V_2O_5, with a capacitance of 3.92 mF cm^{-2} at 10 mV s^{-1}. The capacitance was comparably higher than that of other reported combinations of graphene–MnO_2–Ag, CNTs–carbon–MnO_2, and graphene-CNTs.[164–166] The GCD profile also exhibited a higher capacitance of 2.3 mF cm^{-2} at

a current density of 0.02 mA cm^{-2} (Fig. 10h). The synergistic effect of both V_2O_5 and EG was attributed to enhanced performance, where V_2O_5 acts as a spacer to prevent the aggregation of EG nanosheets in the hybrid film and therefore provides an accessible path for electrolyte ions, while the EG layer improves the electrical conductivity in the system. The electrolyte contains electrochromically active MV^{2+} and therefore drives its redox state during the charging–discharging cycle, giving a clear color, from colorless to purple, in a voltage window from 0 to 1 V. A colored picture of the EG–V_2O_5 MSC signifies the charged state at 1 V, as shown in Fig. 10i, with dark patch like different strips.

An Au/Ag core–shell-embedded PDMS, bistacked WO_3 nanotube–PEDOT:PSS stretchable electrode was designed and converted into a wearable ECS device using a PAAM-based hydrogel electrolyte.[167] This core–shell structure prevents Ag oxidation and maintains electrical conductivity for a long time, even under continuous tensile and bending conditions. The electrochemically active bistacked WO_3–PEDOT:PSS layer provides high performance with mechanical deformation and reflects a maximum capacitance of 471.0 F g^{-1} along with a CE of 83.9 cm^2 C^{-1} for the dual optical window. Recently, a CNT-based hybrid electrode was designed for dual application. The single-walled carbon nanotube (SWCNT)–$W_{18}O_{49}$ NW combination displayed a high surface capacitance of 2 mA cm^{-2} and a volumetric capacitance of 459 F cm^{-3}. However, an asymmetric device designed using SWCNTs–$W_{18}O_{49}$ (as a negative electrode) and SWCNTs–PANI (as a positive electrode) exhibited much higher electrochemical performance, including 95.9% capacitance retention after 6000 cycles and a high energy density of 14.9 mW h cm^{-3}.[179]

Extensive studies have been conducted in order achieve transparent electrodes composed of Au networks, Ag grids, and Ni, which are known for high electrical conductivity. Also, AgNW-based electrodes are promising and cost effective in printable, scalable, and flexible devices. Ginting *et al.* fabricated a novel hybrid AgNW–PEDOT:PSS transparent electrode modified with a conjugated polyelectrolyte blend and $Ni(OH)_2$.[169] The wettability of AgNWs improved with the addition of PEIE, followed by deposition of PEDOT:PSS. This shows that the addition of $Ni(OH)_2$ to PEIE improves the charge transfer and ion diffusion mechanism. A symmetrical solid-state bifunctional ECS device was designed using a Li$^+$-loaded gel electrolyte, as shown in Fig. 11a, under flat and crumple conditions. An 80% transmittance was measured for this solid-state flexible device under neutral conditions. A wide CV curve traced at a 100 mV s^{-1} scan rate with a $Ni(OH)_2$–PEIE composite ECS device showed a large redox current density and provided a quasi-rectangular CV pattern. The areal capacitance of pristine AgNWs–PEDOT:PSS and AgNWs–PEDOT:PSS with a $Ni(OH)_2$–PEIE composite was 2.2 mF cm^{-2} and 3.3 mF cm^{-2}, respectively, at a 10 mV s^{-1} scan rate (Fig. 11b). The GCD of the composite ECS under various current densities (Fig. 11c) also displayed a nearly triangular pattern with good capacitive characteristics. This large electrochemical energy storage property is mainly governed by the presence of pseudocapacitive $Ni(OH)_2$ and a higher surface area of the PEDOT:PSS film. The coloration of the device during charging–discharging cycles also suppresses the transmission by 40%, unless the change appears to be a deep-blue color. An easier path provides for electrolyte penetration, and fast Li$^+$ diffusion at the electrode surface leads to a faster switching speed. Therefore, fast EC switching integrates well with the fast charging–discharging process. Fig. 11d shows a full optical contrast of 27%, which was achieved when the charging level reached 1.6 V at a current density of 80 μA cm^{-2} and manifested noticeable optical changes for the ECS.

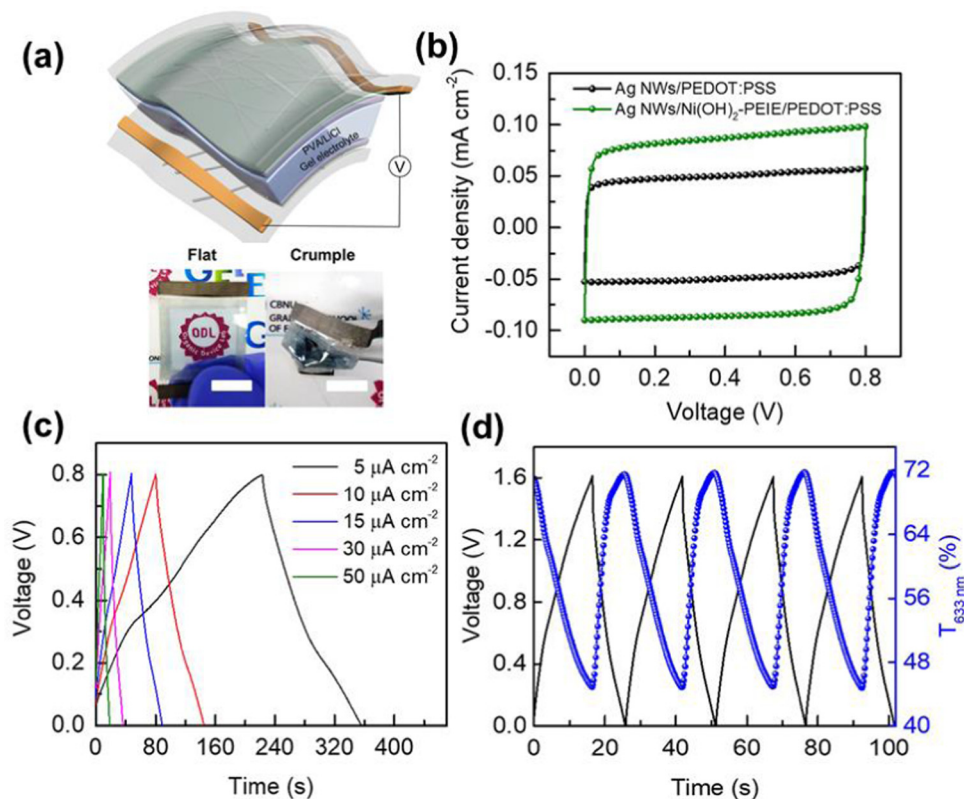**Fig. 11** AgNW−Ni(OH)$_2$−PEIE−PEDOT:PSS device structure under flat and crumple conditions (a). CV measurement of the device with and without the Ni(OH)$_2$ layer (b). GCD pattern of the hybrid ECS with different current densities (c) and synchronized GCD graph and transmission spectra of the device at 80 μA cm^{-2} (d). Permission from ref. 169. Copyright [2018] Elsevier.

4. Electrochromic battery system

The current century is witnessing a growing demand for batteries in practical applications.[180–182] After the discovery of the Li^+ battery, other metal ions (Na^+, K^+, Al^{3+}, Ca^{2+}, Zn^{2+}) have been equally considered for realizing efficient use in energy systems.[183] However, the same characterization of batteries and supercapacitors creates confusion until their full device configuration is not determined. Gogosti *et al.* precisely defined these two charge-storing bodies with their CV and GCD curves, but there is still some overlap when pseudocapacitive behavior is compared with battery characteristics. Some researchers have claimed that EC devices with energy storage property are like batteries instead of ECSs.[95] Transition metal oxides, CPs, organic materials, and, especially, hybrid systems have been explored for designing single-ECB systems. However, there exist some open challenges in terms of specific capacity, stability, CE, and response time, which need to be addressed.

Viologen, an organic electrochromically active material, has recently been used in ECS devices, and some researchers have also applied it in ECB systems. The addition of heavy atoms, such as chalcogens (S, Se, and Te), into viologen moieties improves the capacity and cyclic stability of batteries.[184] A series of benzylated chalcogenoviologens and poly(chalcoviologen)s were synthesized for multiple stable reversible redox centers, and they exhibited strong electron-accepting properties for the EC effect. The introduction of heavier chalcogen atoms substantially enhanced the discharge capacity and stability. The capacitance was 502 mA h g^{-1} at a current density of 100 mA g^{-1} for poly(Te-BnV). This enhancement was summarized by an increment in electrical conductivity and an extra lithiation process on the Te atom.

The fabrication of flexible organic ECB devices was also designed in this system and opens up a new area of energy storage in viologen molecules. A metal electrode and an anion exchange membrane for fabricating a Zn–viologen hybrid battery have been recently explored.[186] The system also carries one additional function of the EC mirror state. The reduction of viologen (V^{2+} to $V^{\bullet +}$) at the cathode side helps deposit Zn atoms at the Zn–ITO electrode *via* electrodeposition. The formation of a mirror state, during charging of the device, possibly converts electrical energy to chemical energy. The stored energy was measured to be 65.0 mA h g^{-1} specific capacity. In addition, a long open-circuit memory effect was also observed in the same system, reaching a high optical reflectance of 84.9%.

Prussian blue was the first inorganic material used as an electrode in a battery system. With advancements in this field, a variety of inorganic materials have been developed, even in single, multifunctional energy storage systems.[187] It is necessary for device engineers to build smart batteries with improved performance based on human readability. Environmentally sustainable and biologically safe electronic devices are being designed with aqueous-compatible materials. Amongst aqueous-based ECBs, Zn is often used due to its low redox potential (-0.76 V *vs.* standard hydrogen electrode [SHE]); in addition, Zn is environmentally friendly, nontoxic, and cost-effective and shows excellent water stability with several distinctive merits. One extra advantage of

having a multivalent charge carrier (Zn^{2+}) is a higher energy density compared to monovalent ions, such as Li^+ and Na^+.[188,189] The combination of Zn-based EC devices is also highlighted due to the colorless state of a Zn^{2+}-containing electrolyte; therefore, the device has neat color visuals during charging and discharging. A coordination polymer iron terpyridyl nanostructure has been rationally designed with a Zn-based system *via* electropolymerization. The incorporation of iron allows for switching between +2 and +3 oxidation states without changing the coordination geometry of the coordination polymer, which is believed to boost its electrochemical process for a prolonged period. A high concentration of a $Zn(ClO_4)_2$ electrolyte is used to eliminate water electrolysis and stretch the working potential window between Zn and Zn^{2+} species. A schematic representation of the device containing coordination polymer-modified and Zn-framed FTO electrodes is shown in Fig. 12a.[185] A high volumetric capacity up to 249.1 mA cm^{-3} was achieved, as shown in Fig. 12b. When the device potential was stepped up to 2.3 V during charging, it showed a dramatic increment in transmission around 572 nm and reverted to its original value of 1.0 V upon discharging. The change in transmission during the charging–discharging process causes a purplish-blue and transparent state for the device, as shown in Fig. 12c and d, with 69% optical change, which is enough to declare the charge level of the coordination polymer-modified ECB.

Recently, Zhang *et al.* found the Zn-based ECB system in a different combination. A prototype aqueous $Zn–V_3O_7$ ECB was constructed by using Zn foils (anode), a V_3O_7 electrode (cathode), and a $ZnSO_4$ aqueous electrolyte. In addition to reversible multicolor switching between yellow, grayish, and blue, the device exhibited an optical contrast of 21% and an energy density of 15.2 mW h g^{-1}. This system also possessed an open-circuit potential of 1.38 V, which enabled the self-coloration and energy retrieval functionality.[190] Improved capacity and EC performance were achieved when the same device was modulated with a Ti-substituted tungsten molybdenum oxide (Mo/Ti:WO_3, MTWO) electrode. This technique used high optical contrast (76%) and a 260 mA h m^{-2} areal capacitance. In short, Ti substitution leads to a sequential exchange of W^{6+}/Mo^{6+} with Ti^{4+}. Due to the similar ionic radii of these ions, a partial substitution of Ti^{4+} occurs at the W^{6+}/Mo^{6+} site and creates a vacant A-site in the original lattice. This vacant A-site provides a rigid channel for Zn^{2+} intercalation in the Zn–MTWO ECB system.[191] Therefore, unlocking the electrochemical active site is a promising method of enhancing performance.

Due to one major concern of high opacity of Zn-based ECBs, where the electrodes are designed with either a Zn frame or a Zn-mesh-like geometry, Sing *et al.* prepared a flexible, transparent Ni@AgNW backbone network to deposit Zn metal. A Zn nanoflake nanofiber network electrode exhibited an optical transparency of ~80% (at 550 nm) with high conductivity and good mechanical strength.[197] In the fabrication of a flexible device, the Zn@Ni@AgNW electrode worked as the anode and the electrodeposited electrochromically active PANI–THE was used as the cathode, along with the polymer gel electrolyte. In terms of performance of this flexible ECB, an
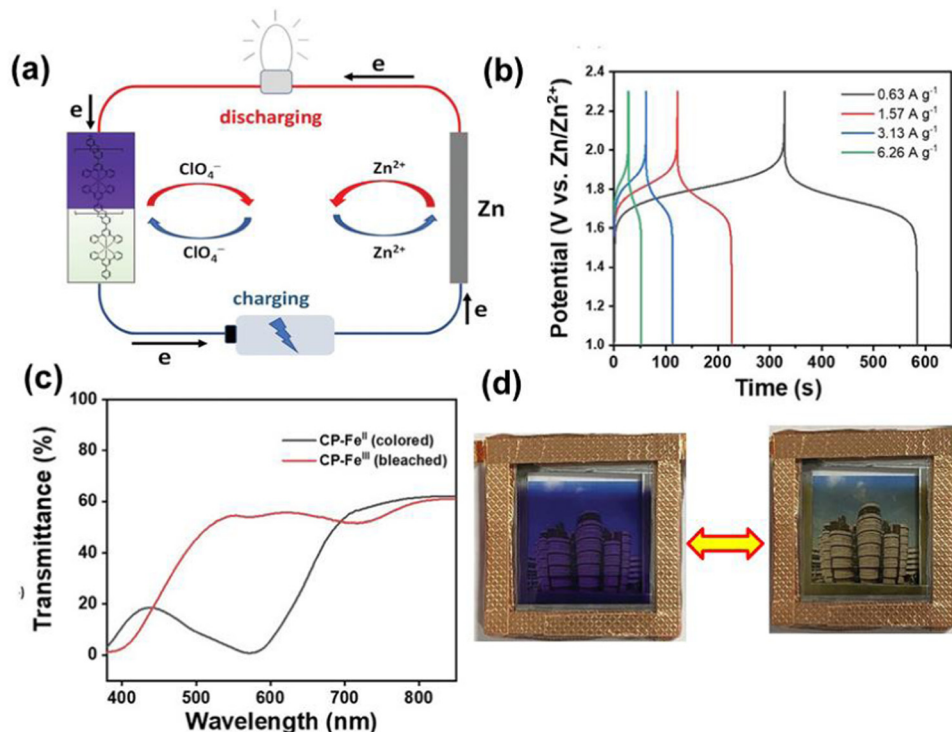
Fig. 12 Schematic design of an electrochromic battery (ECB) in a two-electrode system (a). GCD profile of Zn−ECB with different current densities (b). Changing optical figures during charging through transmittance spectra (c), and the real picture of the ECB during charging−discharging (d). Reproduced from ref. 185. Copyright [2021] Wiley-VCH (open access).

aerial capacity of 174.8 mA h m^{-2} was observed at a current density of 0.013 mA cm^{-2} with a reversible color change from transparent to dark bluish-to-violet upon charging. A transparent Zn-based electrode has an advantage in smart, wearable ECB devices in that any mechanical deformation does not affect device performance. Recently, there have been attempts at creating Al^{3+}, Ca^{2+}, Mg^{2+}, and Li$^+$ ECB systems in a similar pattern to Zn^{2+} ECBs where they exhibit their device operation due to the electrolyte ions rather than metallic anode electrodes like Zn frames.

Ca^{2+} (like Li$^+$) shows a low polarization strength and charge density compared to Mg^{2+}, Zn^{2+}, and Al^{3+} and, therefore, stays away from the kinetic issues caused by multivalent ions having high polarization strength.[200,201] However, the diffusion of metal ions at the electrode surface and a suitable electrolyte are mandatory for designing a high-performance ECB. Therefore, water-in-salt (WIS) electrolytes in EC devices have attracted substantial interest as they exhibit a wide operating potential window, improve the metal ion desolvation kinetics with enhanced anion–cation interactions, and decrease water activity. Different aqueous electrolytes having Na$^+$/k$^+$/Li$^+$/Zn^{2+}/Mg^{2+}/Al^{3+}/Ca^{2+} have already been proposed successfully. Two different aqueous electrolyte-based ECBs having Ca^{2+} and Al^{3+} were successfully fabricated by Tong et al.[192,193] However, the anode electrode was kept different for these two systems. Fig. 13a shows one ECB system fabricated with amorphous vanadium oxide (VO$_x$ as the anode) and indium hexacyanoferrate (lnHCF as the cathode) electrodes. An aqueous Ca^{2+}-based Ca(OTF)$_2$ electrolyte was used for designing this ECB. The anodic electrode showed chromic

modulation from a greenish-yellow color to black under the alteration of redox states V^{3+}/V^{4+} and V^{4+}/V^{5+}. Because of the high rate of Ca^{2+} insertion/extraction, a yellow-to-colorless film developed at the cathode. The rational design explored the EC effect from yellow to black during charging (where Ca^{2+} was inserted at the cathode surface), as shown in Fig. 13b. An excellent energy density of 51.4 mW h m^{-2} at a power density of 1737.3 mW m^{-2} was measured in this case. Therefore, a complete charge–discharge cycle with a color change of an aqueous Ca^{2+} based ECB exhibits high transmittance modulation at a current density of 0.1 mA cm^{-2}, as shown in Fig. 13c.

Similarly, an Al^{3+}-based aqueous ECB was designed with amorphous WO$_3$ (anode) and InHCF (cathode) electrodes having a WIS aluminum triflate [Al(OTF)$_3$] electrolyte, as shown in Fig. 13d. It was believed that due to the small radius of Al^{3+}, it can deliver three electron redox states and hence lead to high energy density. However, the kinetics of Al^{3+} diffusion in electrolytes is more sluggish to operate. Therefore, to improve electrochemical stability, a water-based electrolyte [Al(OTF)$_3$] was chosen. A stable charge–discharge profile of the Al^{3+} ECB was observed under 0–1.4 V, as shown in Fig. 13e, with different current densities and showed an impressive energy density of 62.8 mW h m^{-2} at a power density of 2433.8 mW m^{-2}, with excellent high rate and high stability. Due to the presence of electrochromically active electrodes at both ends, a transparent-to-deep-blue color state successfully integrated with the battery function during charging and reflected an optical contrast of $\sim$70–80%, as shown in Fig. 13f. This high coloration contrast
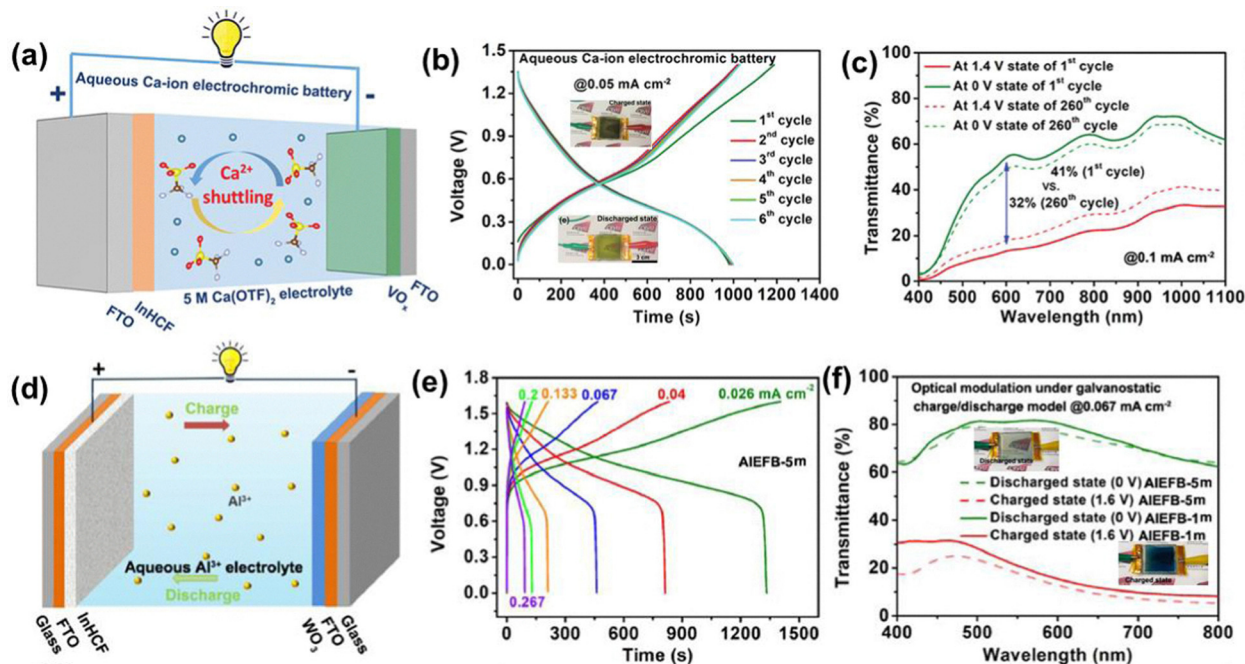
Fig. 13 Two-electrode aqueous Ca^{2+}-based ECB, FTO–lnHCF–$Ca(OTF)_2$–VO_x–FTO (a). Charging–discharging (b) and transmittance spectra of the device during colored and bleached states with different cycles (c). Reproduced from ref. 192. Copyright [2021] Wiley-VCH. Two-electrode aqueous Al^{3+}-based ECB, FTO–lnHCF–$[Al(OTF)_3]$–WO_3–FTO (d). Charging–discharging (e) and transmittance spectra of the ECB with blue and transparent states (f). Reproduced from ref. 193. Copyright [2022] Elsevier.

and fast switching of the device are successfully defined by the aqueous-based Al^{3+} ECB system. Recently, the challenges in both Zn^{2+}- and Al^{3+}-based aqueous ECBs have been rectified by designing a prototype Zn^{2+}–Al^{3+} hybrid system, in which the poor kinetics of Zn^{2+} and Al^{3+} that creates a high redox potential in an aqueous medium has been addressed effectively.[198] Therefore, WO_3 (cathode) in the hybrid Zn^{2+}/Al^{3+} electrolyte system exhibits a high discharge capacity of 185.6 mA h m^{-2} at a current density of 0.5 mA cm^{-2}. The combination also promotes an excellent optical contrast of 88% with a fast response time (<5 s) between the blue and the transparent color state. A similar transparent-to-blue color visualization of ECBs was explored in a $Li_4Ti_5O_{12}$ (cathode)/Prussian white (anode) system with a Li^+ electrolyte. The cathode changed its state from $Li_4Ti_5O_{12}$ to $Li_7Ti_5O_{12}$ by capturing an electron and delivered a deep-blue color state; simultaneously, Li^+ extraction caused a change from Prussian white to Prussian blue.[196] Therefore, a change in optical modulation from transparent to blue ($\sim 55.3\%$) was noticed during charging in a wide potential window. Hence, this ECB system also exhibits a high energy density of 127.2 mW h cm^{-2} and an exceptionally high power density of 24 mW cm^{-2}. The recent progress in the ECB system with parameters is summarized in Table 4.

5. Self-powered EC energy storage device assembly

In the light of recent developments, there is a new potential demand for the ability to harvest and store energy in EC

devices, where any EC device would be considered for consumption of external power. This means that an ECS/ECB cannot store charge or cannot show any optical modulation until an electrical signal input is applied; therefore, the whole system will not be considered for energy saving. Different forms of energy are transformed into electrical energy or used to perform the chemical reaction for an electrochemical ECS/ECB device.[202] ECSs have been recently designed with photovoltaic, thermoelectric, triboelectric, and piezoelectric arrangements to stimulate the chemical reaction in the device *via* natural energy sources.[170,203–206] For example, dye-sensitized solar cells (DSSCs) help convert heat radiation to electrical energy,[207,208] while the triboelectric system converts mechanical energy inputs to electrical energy. A few recent reports on these two systems with tailored ECS functions are described in this section.

Self-charging without any external electrical input is the strength of triboelectric nanogenerator (TENG) devices. Guo *et al.* designed a sliding-mode direct current (DC)-TENG coupled with a PANI-based electrochromically active solid ECS device.[209] A symmetrical PANI-based electrode (with "BINN" patterned in the top electrode and "TENG" patterned in the bottom electrode) was prepared with a PAAM-LiCl hydrogel electrolyte. When realizing the self-charging function of the DC-TENG, a dielectric breakdown occurs for electrification due to the mechanical sliding motion and was implemented on a symmetrical PANI based ECS device, as shown schematically in Fig. 14a. A repeated reciprocal sliding motion was tested on the TENG/Cu electrode, which delivered a pulsed DC output, because no potential difference was generated during reverse sliding. A tribo-electrification layer was provided by one of the

polyethylene-naphthalate (PEN) films in the ECS device, and the slider on the top of the electrode was adjusted accordingly. Continuous sliding of the slider automatically charged the device, and its changing potential profile is plotted in Fig. 14b. If the potential changes across the electrochromically active materials, their corresponding optical modulation must be visible. Therefore, as shown in Fig. 14c, the optical images are reflecting the respective letters of the top/bottom pattern. The device was changed to 0.8 V, due to dynamic doping, when the slider was moved at a speed of 2.7 m s^{-1}. Due to charging of the top electrode, ''BINN'' was clearly seen in the device. Under discharging of the ECS, a blurred image of ''TENG'' and ''BINN'' could be seen with de-doping at 0 V. Under a reverse-sliding scan, a reverse charging current flowed between the electrodes; therefore, the EC effect from the bottom electrode was perceived with ''TENG'' on reaching −0.8 V. Hence, the sliding mechanical motion indicates complete working of a single-ECS device.

The same research group recently designed a hybrid piezo-/triboelectric-driven ECS. Fig. 14d shows the schematic of the device, which contains two primary components: one is an EC μ-SC based on AgNW/NiO active material, and the other is a hybrid arc-shaped tribo-/piezoelectric nanogenerator (NG) shown in the zoomed image of the top and bottom portions of the device.[210] A piezoelectric NG was designed using ITO/P(VDF-TrFE)/Ag (vinylidene fluoride-*co*-trifluoroethylene) and a contact separation mode triboelectric NG with Ag–PTFE–Ag (polytetrafluoroethylene). The vertical coupling of both NGs to an arched shape shares the same Ag electrode, while the bottom piezoelectric NG is used to drive the triboelectric system. The impact of human palms, when undergoing a periodic mechanical deformation on an integrated EC μ-SC device, charges the device to 1 V, and the charging level is visualized by the color change from the NiO electrode with transparent-to-dark-color modulation. This chromic modulation is due to the faradaic redox reaction between Ni^{2+} and Ni^{3+}. Therefore, a continuous palm impact generates an increasing voltage from 0.05 to 1 V in 260 s, as shown in Fig. 14e with color variation of the device. To indicate self-charging, a frequent palm impact was imposed on the device for 30 s, and the regular self-charging status was identified, as shown in Fig. 14f with a different EC color intensity. The operation exhibited a high capacitance of 3.47 mF cm^{-2} and stable cycling performance (80.7% for 10 000 cycles). Therefore, self-charging is successfully conducted with a continuous mechanical impact in this piezo-/triboelectric ECS device and promotes the development of a sustainable, self-powered system for energy harvesting and storage.

Similarly, a self-powered ECS system has been explored with the integration of the device into photovoltaic cells (or DSSCs), which transform solar energy into electrical energy to realize self-powered operation.[212] Sandwich configurations of such devices have recently been investigated in a different set of EC materials, where one integrated DSSC (screen-printed TiO$_2$ film) was designed for a solar energy converter. Xie *et al.* proposed the integration of DSSCs in a WO$_3$ nanoparticle EC device, where the DSSCs absorbed sunlight and converted it to electrical energy to regulate the optical transmission of the WO$_3$ film.[24] The high color contrast of the blue color was driven by the DSSCs, and the extended version of the assigned system delivered a high areal capacitance of 22 mF cm^{-2} with reversible color changing. Since energy generation in a photovoltaic

Table 4 ECB^a system and performance

Number	ECB electrodes	Electrolyte	Chromic modulation		ECB device performance		Ref.
			Charging	Discharging	Optical	Electrical	
1	Zn–ITO^b//ITO	ZnSO$_4$ + viologen	Mirror state	Transparent	$\Delta R \approx 84.9\%$	65.0 mA h g^{-1}	186
2	Poly(Te-BnV)	Lithium hexafluorophosphate	Red	Purple	—	684 mA h g^{-1} at 100 mA g^{-1}	184
3	Zn frame//iron terpyridyl	Zn(ClO$_4$)$_2$	Blue	Transparent	$\Delta T \approx 69\%$	14.5 mA h m^{-2} at 0.02 mA cm^{-2}	185
4	VO$_x$//InHCF	WIS^c Ca(OTF)$_2$ electrolyte	Greenish-black	Greenish-yellow	$\Delta T \approx 78\%$	51.4 mW h m^{-2} at 1737.3 mW m^{-2}	192
5	WO$_3$//InHCF	WIS Al(OTF)$_3$ electrolyte	Blue	Transparent	$\Delta T \approx 65\%$	104.6 mW h m^{-2} at 282.1 mW m^{-2}	193
6	PPy^d film–Al sheet	KCl solution	Black	Yellow	$\Delta T \approx 59.0\%$	75.25 mA h g^{-1} at 1.0 A g^{-1}	194
7	Zn//PPy	KCl–Zn(CH$_3$COO)$_2$	Black	Yellow	—	123 mA h g^{-1}	195
8	Prussian white–Li$_4$Ti$_5$O$_{12}$	LiClO$_4$	Blue	Transparent	$\Delta T \approx 55.3\%$ (170 cm^2 C^1)	127.2 mW h cm^{-2} at and 24 mW cm^{-2}	196
9	Zn@Ni@AgNFs//PANI^e–THE	ZnCl$_2$	Dark bluish-violet	Transparent	$\Delta T \approx 50\%$	174.82 mA h m^{-2} at 0.013 A cm^{-2}	197
10	WO$_3$–Zn–WO$_3$	ZnSo$_4$–AlCl$_3$	Blue	Transparent	$\Delta T \approx 88\%$	185.6 mA h m^{-2} at 0.5 mA cm^{-2}	198
11	V$_3$O$_7$–Zn–V$_3$O$_7$	ZnSO$_4$	Yellow	Grayish-blue	$\Delta T \approx 21\%$	32.6 mW h m^{-2}	190
12	Zn–MTWO	ZnSO$_4$	Dark blue	Transparent	$\Delta T \approx 76\%$	260 mA h m^{-2}	191
13	Microporous pTTpATA polymer	TBAPF6	Red/deep red/blue	Blue/deep red/red	—	81 mA h g^{-1}	104
14	Zn–PB	ZnSO$_4$–KCl	Blue/light blue	Transparent	$\Delta T \approx 83\%$	35.7 mW h m^{-2}	199

^{a} ECB: electrochromic battery. ^{b} ITO: indium doped tin oxide. ^{c} WIS: water-in-salt. ^{d} PPy: polypyrrole. ^{e} PANI: polyaniline.
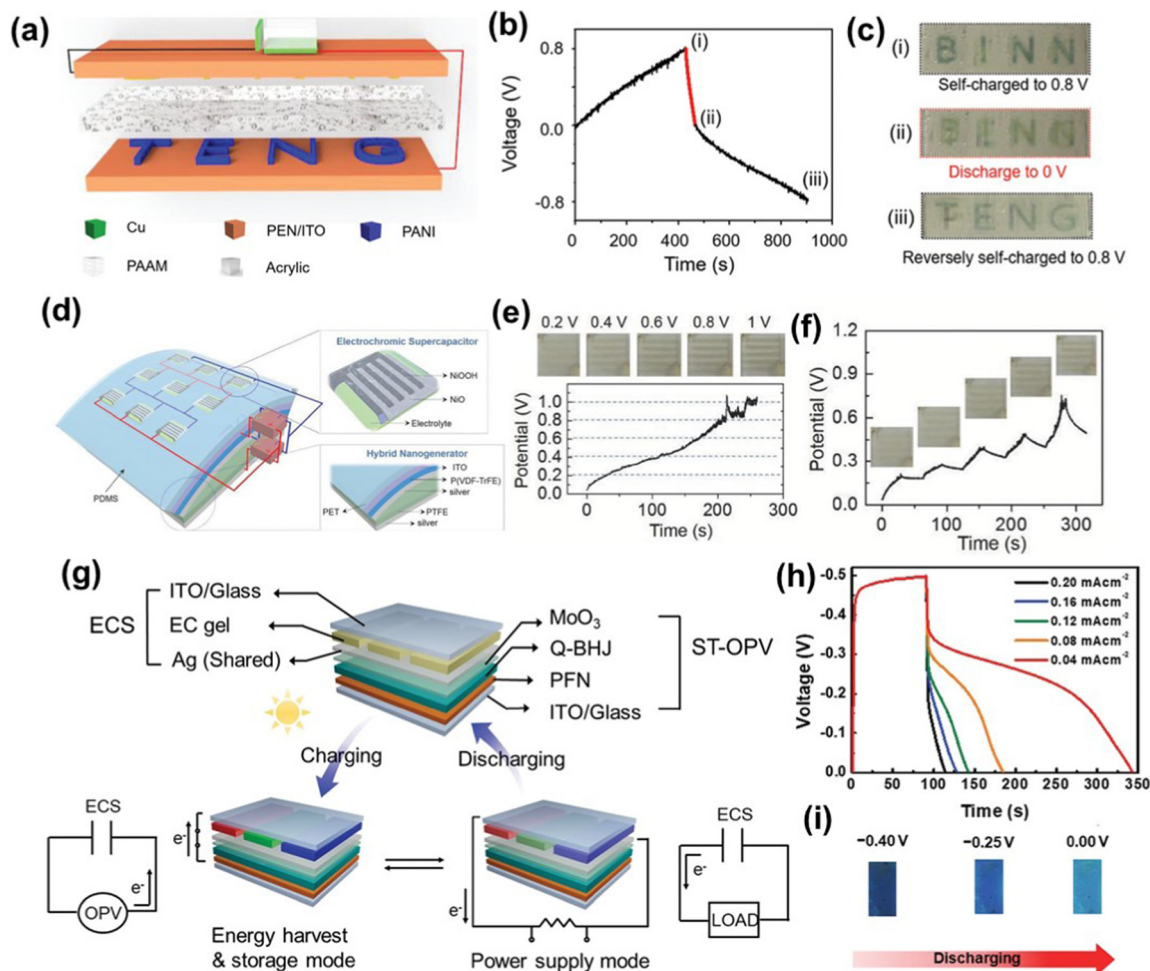
Fig. 14 Schematic illustration of a self-charging electrochromic supercapacitor device (SC-ESCD) (a); changing voltage profiles of the ESCD when being self-charged to 0.8 V by sliding motion, discharged to 0 V using a constant current at 50 μA (b); and corresponding photograph of the device with sliding motion (c). Reproduced from ref. 209. Copyright [2021] Wiley-VCH. Schematic of the SC-ECS, with μ-SC (top inset) and hybrid nanogenerator (NG) (bottom inset) (d). Real-time charged voltage of the EC μ-SC by the hybrid NG under palm impact and chromic transition (top panel) (e). Self-charging process of the EC μ-SC under continuous palm impact (f). Reproduced from ref. 210. Copyright [2018] Wiley-VCH. Schematic device geometry of a monolithically integrated photovoltaic ECS and the two operation modes of the energy-storing functional photovoltaics: energy harvest/storage mode and power supply mode (g). GCD characteristics with different load current densities (h) and different color intensities of the device during discharging (i). Reproduced from ref. 211. Copyright [2020] Wiley-VCH.

cell depends on the intensity of incident light, surplus energy generated can be varied according to the variation of intensity. It is also possible for energy to be dissipated which can depend on the path distance between the storage devices and the energy source.[213,214] Therefore, Cho *et al.* designed a mono-lithically integrated system for energy harvesting and storage in one complete device-based system.[211] One-body assembly of a Q-ST-OPV and ECS works for generating a photocurrent under the exposure of direct sunlight and artificial indoor light, as shown in Fig. 14g. The stored energy is reflected in blue color due to the presence of CF_3-PV^{2+} active chromophores. A photo-voltaic cell is fully charged under LED light irradiation for 91 s, and hence, the energy is successfully delivered to the integrated ECS for charging. The stored energy can be taken out on discharging with different current densities and reflects an aerial capacitance of 26.2 and 18.8 mF cm^{-2} at a current density

of 0.04 mA cm^{-2} and 0.2 mA cm^{-2}, respectively, as shown in Fig. 14h. The discharging status is visualized by different blue color intensity, as shown in Fig. 14i. Color modification can also be achieved by varying the composition of the photoactive material. Overall, these different breakthroughs describe the attempts that have been made in energy harvesting and storage by incorporating EC energy storage functions.

6. Summary and future perspective

This minireview focused on the recent progress in multifunc-tional EC materials in a single energy storage system. EC materials belonging to organic, inorganic, and CP families are well suited for energy storage. In a similar device configu-ration, reversible redox reactions at both electrode surfaces

make it possible to store energy in terms of color visuals. Therefore, by looking at the device color, we can estimate how much energy is stored. However, there is an inherent disadvantage in that these materials exhibit limited colors. In contrast, a hybrid structure and F–P cavity-type reflective devices with inorganic materials possibly provide multiple color states. Modifying electrodes with ultrahigh porous structures, varying the doping concentration, and controlling film thickness are easy ways to enhance the electrochemical performance of inorganic materials. Polymers and organic materials are also developed in multicolor states. Polymers are designed with various donor and acceptor units for excellent charge transportation. To make a planer polymer film electrode, π-spacers are introduced between the polymer chains, which restrict agglomeration, tuning the morphology. Additionally, pseudo factors, such as charge transfer resistance and interfacial resistance (electrode sheet resistance, electrode–electrolyte interface) of high magnitude, also contribute to energy dissipation, and taking appropriate measures can increase device performance. In addition, transformation from liquid electrolytes to polymer ion gel electrolytes improves charge transportation, as well as helps stretch the operating potential window, leading to a higher energy density and power density. One additional advantage of ion gel electrolytes is that they operate successfully in a high-temperature range and under adverse strain conditions. Different flexible, foldable, screen-printed, tattoo like EC energy storage devices are fabricated using suitably designed electrodes and electrolytes.

In contrast to ECSs, whose properties are principally determined by the electrode, the ECB system is influenced by both electrolyte ions and the nature of the electrode. However, with increasing demand for the replacement of Li^+ battery systems, metal ions Ca^{2+}, Al^{3+}, and Zn^{2+} are used in ECBs in different suitable combinations. Multivalent ions, a low ionic radius, fast kinetics, and low polarization strength are required for excellent performance. Mixed-valence hybrid cations are well established in aqueous electrolyte systems to eliminate the high redox potential of the electrochemical cell. In addition, a self-powered system is an important feature of future technology. ECS and ECB systems store energy when directly connected to external electrical inputs. However, there have been innovations such as self-charging devices for energy harvesting technology. Photovoltaics, TENGs, PENGs, and solar-driven systems convert energy into electrical energy, which is then applied to EC devices and contributes to energy storage. Sharing one electrode for multitasking applications in a self-powered system is an efficient strategy for low-cost green energy saving. Monolithically designed self-powered EC systems also prevent energy loss by constructing an efficient, smart device.

Multiple color states, a fast response, a high CE, high optical contrast, a high energy density, and a low operational redox potential are the elementary requirements of an efficient, smart, multifunctional EC energy storage device. Designing a futuristic EC energy storage device that fixes all these parameters is a challenge for engineers. EC energy storage devices currently use laminated structures, and their interfaces are prone to structural change, resulting in performance degradation. A stretchable, flexible, deformable, self-healing, durable, and low-cost EC energy storage system is still an open question for future real-world application. Technologies where electrodes/devices would retain conductivity and transparency under regular mechanical impact should be the focus of research. Energy related to random human motions in daily life can be interlinked to EC energy storage devices for manufacturing the next generation clean energy devices. With growing interest, EC memory and EC mirrors are also possible avenues to design multiple embedded applications of EC devices in the same electrochemical unit. Throughout this minireview, we have attempted to give short glimpses of the recent progress in EC energy storage systems. We hope that this minireview will contribute to a better understanding for achieving many relevant potential improvements for the future.

Conflicts of interest

There are no conflicts to declare.

Acknowledgements

References

1 C. G. Granqvist, *Handbook of Inorganic Electrochromic Materials, Elsevier, Amsterdam, The Netherland*s, 1995, reprinted 2002.

2 R. J. Mortimer, *Chem. Soc. Rev.*, 1997, **26**, 147–156.

3 P. R. Somani and S. Radhakrishnan, *Mater. Chem. Phys.*, 2003, **77**, 117–133.

4 J. Peng, H. H. Jeong, Q. Lin, S. Cormier, H. L. Liang, M. F. L. D. Volder, S. Vignolini and J. J. Baumberg, *Sci. Adv.*, 2019, **5**, 2205.

5 G. J. Stec, A. Lauchner, Y. Cui, P. Nordlander and N. J. Halas, *ACS Nano*, 2017, **11**, 3254–3261.

6 D. R. Rosseinsky and R. J. Mortimer, *Adv. Mater.*, 2001, **13**, 783–793.

7 R. J. Mortimer, A. L. Dyer and J. R. Reynolds, *Displays*, 2006, **27**, 2–18.

8 J. R. Platt, *J. Chem. Phys.*, 1961, **34**, 862–863.

9 G. Cai, J. Wang and P. S. Lee, *Acc. Chem. Res.*, 2016, **49**, 1469–1476.

10 G. Yang, Y.-M. Zhang, Y. Cai, B. Yang, C. Gu and S. X.-A. Zhang, *Chem. Soc. Rev.*, 2020, **49**, 8687–8720.

11 Z. Wang, X. Wang, S. Cong, F. Geng and Z. Zhao, *Mater. Sci. Eng., R*, 2020, **140**, 100524.

12 Y. R. In, Y. M. Kim, Y. Lee, W. Y. Choi, S. H. Kim, S. W. Lee and H. C. Moon, *ACS Appl. Mater. Interfaces*, 2020, **12**, 30635–30642.

13 A. Chaudhary, D. K. Pathak, M. Tanwar, J. Koch, H. Pfnür and R. Kumar, *J. Mater. Chem. C*, 2020, **8**, 1773–1780.

14 Y. Rao, J. Dai, C. Sui, Y.-T. Lai, Z. Li, H. Fang, X. Li, W. Li and P.-C. Hsu, *ACS Energy Lett.*, 2021, **6**, 3906–3915.

15 X. Guo, J. Chen, A. L.-S. Eh, W. C. Poh, F. Jiang, F. Jiang, J. Chen and P. S. Lee, *ACS Appl. Mater. Interfaces*, 2022, **14**, 20237–20246.

16 P. Yang, P. Sun and W. Mai, *Mater. Today*, 2016, **19**, 394–402.

17 A. L.-S. Eh, J. Chen, X. Zhou, J.-H. Ciou and P. S. Lee, *ACS Energy Lett.*, 2021, **6**, 4328–4335.

18 Y. Xia, *ACS Cent. Sci.*, 2020, **6**, 2130–2132.

19 C. Wang, X. Jiang, P. Cui, M. Sheng, X. Gong, L. Zhang and S. Fu, *ACS Appl. Mater. Interfaces*, 2021, **13**, 12313–12321.

20 Y. Shi, M. Sun, Y. Zhang, J. Cui, X. Shu, Y. Wang, Y. Qin, J. Liu, H. H. Tan and Y. Wu, *ACS Appl. Mater. Interfaces*, 2020, **12**, 32658–32665.

21 W. Wu, L. Wu, H. Ma, L. Wu, H. Wang and H. Fang, *Chem. Eng. J.*, 2022, **446**, 137122.

22 C. J. Schoot, J. J. Ponjee, H. T. van Dam, R. A. van Doorn and P. T. Bolwijn, *Appl. Phys. Lett.*, 1973, **23**, 64–65.

23 R. J. Mortimer, *Annu. Rev. Mater. Res.*, 2011, **41**, 241–268.

24 Z. Xie, X. Jin, G. Chen, J. Xu, D. Chen and G. Shen, *Chem. Commun.*, 2014, **50**, 608–610.

25 J. Koo, V. Amoli, S. Y. Kim, C. Lee, J. Kim, S.-M. Park, J. Kim, J. M. Ahn, K. J. Jung and D. H. Kim, *Nano Energy*, 2020, **78**, 105199.

26 K. Chen, J. He, D. Zhang, L. You, X. Li, H. Wang and J. Mei, *Nano Lett.*, 2021, **21**, 4500–4507.

27 A. M. Österholm, L. Nhon, D. Eric Shen, A. M. Dejneka, A. L. Tomlinson and J. R. Reynolds, *Mater. Horiz.*, 2022, **9**, 252–260.

28 L. Wang, M. Guo, J. Zhan, X. Jiao, D. Chen and T. Wang, *J. Mater. Chem. A*, 2020, **8**, 17098–17105.

29 H. Wang, C.-J. Yao, H.-J. Nie, L. Yang, S. Mei and Q. Zhang, *J. Mater. Chem. C*, 2020, **8**, 15507–15525.

30 X. Yang, G. Zhu, S. Wang, R. Zhang, L. Lin, W. Wu and Z. Lin Wang, *Energy Environ. Sci.*, 2012, **5**, 9462–9466.

31 J. Wang, L. Zhang, L. Yu, Z. Jiao, H. Xie, X. W. (David) Lou and X. W. Sun, *Nat. Commun.*, 2014, **5**, 1–7.

32 M. Qiu, F. Zhou, P. Sun, X. Chen, C. Zhao and W. Mai, *Nano Energy*, 2020, **78**, 105148.

33 S.-H. Lee, H. M. Cheong, J.-G. Zhang, A. Mascarenhas, D. K. Benson and S. K. Deb, *Appl. Phys. Lett.*, 1999, **74**, 242–244.

34 A. Chaudhary, D. K. Pathak, M. Tanwar and R. Kumar, *Anal. Chem.*, 2020, **92**, 6088–6093.

35 D. S. Dalavi, R. S. Desai and P. S. Patil, *J. Mater. Chem. A*, 2022, **10**, 1179–1226.

36 J. K. Lee, Y. M. Kim and H. C. Moon, *Macromol. Rapid Commun.*, 2021, **42**, 2100468.

37 Y. M. Kim, X. Li, K.-W. Kim, S. H. Kim and H. C. Moon, *RSC Adv.*, 2019, **9**, 19450–19456.

38 B. Gélinas, D. Das and D. Rochefort, *ACS Appl. Mater. Interfaces*, 2017, **9**, 28726–28736.

39 V. H. V. Quy, K.-W. Kim, J. Yeo, X. Tang, Y. R. In, C. Jung, S. M. Oh, S. J. Kim, S. W. Lee, H. C. Moon and S. H. Kim, *Org. Electron.*, 2022, **100**, 106395.

40 H. Oh, J. K. Lee, Y. M. Kim, T. Y. Yun, U. Jeong and H. C. Moon, *ACS Appl. Mater. Interfaces*, 2019, **11**, 45959–45968.

41 H. C. Moon, T. P. Lodge and C. D. Frisbie, *Chem. Mater.*, 2015, **27**, 1420–1425.

42 M. Kathiresan, L. Walder, F. Ye and H. Reuter, *Tetrahedron Lett.*, 2010, **51**, 2188–2192.

43 B. Evanko, S. J. Yoo, S.-E. Chun, X. Wang, X. Ji, S. W. Boettcher and G. D. Stucky, *J. Am. Chem. Soc.*, 2016, **138**, 9373–9376.

44 K. Moon and A. E. Kaifer, *Org. Lett.*, 2004, **6**, 185–188.

45 K. Madasamy, D. Velayutham, V. Suryanarayanan, M. Kathiresan and K.-C. Ho, *J. Mater. Chem. C*, 2019, **7**, 4622–4637.

46 C. L. Bird and A. T. Kuhn, *Chem. Soc. Rev.*, 1981, **10**, 49–82.

47 H. Oh, D. G. Seo, T. Y. Yun, C. Y. Kim and H. C. Moon, *ACS Appl. Mater. Interfaces*, 2017, **9**, 7658–7665.

48 D.-C. Huang, J.-T. Wu, Y.-Z. Fan and G.-S. Liou, *J. Mater. Chem. C*, 2017, **5**, 9370–9375.

49 T. Welton, *Chem. Rev.*, 1999, **99**, 2071–2084.

50 M. Kathiresan and D. Velayutham, *Chem. Commun.*, 2015, **51**, 17499–17516.

51 Y.-S. Ye, J. Rick and B.-J. Hwang, *J. Mater. Chem. A*, 2013, **1**, 2719–2743.

52 B. Lu, S. Zhen, S. Zhang, J. Xu and G. Zhao, *Polym. Chem.*, 2014, **5**, 4896–4908.

53 M. Jaiswal and R. Menon, *Polym. Int.*, 2006, **55**, 1371–1384.

54 G. A. Sotzing, J. R. Reynolds and P. J. Steel, *Chem. Mater.*, 1996, **8**, 882–889.

55 S. Ming, Z. Li, S. Zhen, P. Liu, F. Jiang, G. Nie and J. Xu, *Chem. Eng. J.*, 2020, **390**, 124572.

56 W. Zhang, H. Li, E. Hopmann and A. Y. Elezzabi, *Nanophotonics*, 2021, **10**, 825–850.

57 G. Cai, J. Tu, C. Gu, J. Zhang, J. Chen, D. Zhou, S. Shi and X. Wang, *J. Mater. Chem. A*, 2013, **1**, 4286–4292.

58 T. Y. Yun, X. Li, J. Bae, S. H. Kim and H. C. Moon, *Mater. Des.*, 2019, **162**, 45–51.

59 R. Kumar, D. K. Pathak and A. Chaudhary, *J. Phys. D: Appl. Phys.*, 2021, **54**, 503002.

60 C. G. Granqvist, *Sol. Energy Mater. Sol. Cells*, 2012, **99**, 1–13.

61 J. Livage and D. Ganguli, *Sol. Energy Mater. Sol. Cells*, 2001, **68**, 365–381.

62 J. Wang, E. Khoo, P. S. Lee and J. Ma, *J. Phys. Chem. C*, 2008, **112**, 14306–14312.

63 P. Salles, D. Pinto, K. Hantanasirisakul, K. Maleski, C. E. Shuck and Y. Gogotsi, *Adv. Funct. Mater.*, 2019, **29**, 1809223.

64 G. Valurouthu, K. Maleski, N. Kurra, M. Han, K. Hantanasirisakul, A. Sarycheva and Y. Gogotsi, *Nanoscale*, 2020, **12**, 14204–14212.

65 D. K. Pathak, A. Chaudhary, M. Tanwar, U. K. Goutam and R. Kumar, *Appl. Phys. Lett.*, 2020, **116**, 141901.

66 V. K. Thakur, G. Ding, J. Ma, P. S. Lee and X. Lu, *Adv. Mater.*, 2012, **24**, 4071–4096.

67 C. Dulgerbaki, N. N. Maslakci, A. I. Komur and A. U. Oksuz, *Eur. Polym. J.*, 2018, **107**, 173–180.

68 S. Xiong, S. Yin, Y. Wang, Z. Kong, J. Lan, R. Zhang, M. Gong, B. Wu, J. Chu and X. Wang, *Mater. Sci. Eng., B*, 2017, **221**, 41–53.

69 J. Zhang, J. Tu, D. Zhang, Y. Qiao, X. Xia, X. Wang and C. Gu, *J. Mater. Chem.*, 2011, **21**, 17316–17324.

70 J. Zhu, S. Wei, M. Jr. Alexander, T. D. Dang, T. C. Ho and Z. Guo, *Adv. Funct. Mater.*, 2010, **20**, 3076–3084.

71 D. M. DeLongchamp and P. T. Hammond, *Chem. Mater.*, 2004, **16**, 4799–4805.

72 Y. Shi, Y. Zhang, K. Tang, J. Cui, X. Shu, Y. Wang, J. Liu, Y. Jiang, H. H. Tan and Y. Wu, *Chem. Eng. J.*, 2019, **355**, 942–951.

73 J. Zhang, J. Tu, G. Du, Z. Dong, Y. Wu, L. Chang, D. Xie, G. Cai and X. Wang, *Sol. Energy Mater. Sol. Cells*, 2013, **114**, 31–37.

74 H. Ling, L. Liu, P. S. Lee, D. Mandler and X. Lu, *Electrochim. Acta*, 2015, **174**, 57–65.

75 H. Li, L. McRae and A. Y. Elezzabi, *ACS Appl. Mater. Interfaces*, 2018, **10**, 10520–10527.

76 S. Zhang, S. Chen, F. Yang, F. Hu, B. Yan, Y. Gu, H. Jiang, Y. Cao and M. Xiang, *Org. Electron.*, 2019, **65**, 341–348.

77 S. Xiong, Y. Xiao, J. Ma, L. Zhang and X. Lu, *Macromol. Rapid Commun.*, 2007, **28**, 281–285.

78 J. Wei, S. Xiong, Y. Bai, P. Jia, J. Ma and X. Lu, *Sol. Energy Mater. Sol. Cells*, 2012, **99**, 141–147.

79 P. Jia, A. A. Argun, J. Xu, S. Xiong, J. Ma, P. T. Hammond and X. Lu, *Chem. Mater.*, 2009, **21**, 4434–4441.

80 S. Xiong, J. Wei, P. Jia, L. Yang, J. Ma and X. Lu, *ACS Appl. Mater. Interfaces*, 2011, **3**, 782–788.

81 G. Krieger and B. Tieke, *Macromol. Chem. Phys.*, 2017, **218**, 1700052.

82 S. Napierała and M. Wałęsa-Chorab, *Eur. Polym. J.*, 2020, **140**, 110052.

83 A. Bandyopadhyay and M. Higuchi, *Eur. Polym. J.*, 2013, **49**, 1688–1697.

84 S. Napierała, M. Kubicki and M. Wałęsa-Chorab, *Inorg. Chem.*, 2021, **60**, 14011–14021.

85 I. Mukkatt, A. P. Mohanachandran, A. Nirmala, D. Patra, P. A. Sukumaran, R. S. Pillai, R. B. Rakhi, S. Shankar and A. Ajayaghosh, *ACS Appl. Mater. Interfaces*, 2022, **14**, 31900–31910.

86 M. K. Bera, S. Mohanty, S. S. Kashyap and S. Sarmah, *Coord. Chem. Rev.*, 2022, **454**, 214353.

87 R. Sakamoto, K. Takada, X. Sun, T. Pal, T. Tsukamoto, E. J. H. Phua, A. Rapakousiou, K. Hoshiko and H. Nishihara, *Coord. Chem. Rev.*, 2016, **320–321**, 118–128.

88 C. Lambert and G. Nöll, *Angew. Chem., Int. Ed.*, 1998, **37**, 2107–2110.

89 Q. Hao, Z.-J. Li, C. Lu, B. Sun, Y.-W. Zhong, L.-J. Wan and D. Wang, *J. Am. Chem. Soc.*, 2019, **141**, 19831–19838.

90 A. L.-S. Eh, A. W. M. Tan, X. Cheng, S. Magdassi and P. S. Lee, *Energy Technol.*, 2018, **6**, 33–45.

91 W. Li, T. Bai, G. Fu, Q. Zhang, J. Liu, H. Wang, Y. Sun and H. Yan, *Sol. Energy Mater. Sol. Cells*, 2022, **240**, 111709.

92 J.-L. Wang, S.-Z. Sheng, Z. He, R. Wang, Z. Pan, H.-Y. Zhao, J.-W. Liu and S.-H. Yu, *Nano Lett.*, 2021, **21**, 9976–9982.

93 J. Kim, J. Lee, J. You, M.-S. Park, M. S. Al Hossain, Y. Yamauchi and J. Ho Kim, *Mater. Horiz.*, 2016, **3**, 517–535.

94 W. Raza, F. Ali, N. Raza, Y. Luo, K.-H. Kim, J. Yang, S. Kumar, A. Mehmood and E. E. Kwon, *Nano Energy*, 2018, **52**, 441–473.

95 Y. Gogotsi and R. M. Penner, *ACS Nano*, 2018, **12**, 2081–2083.

96 S. Sathyamoorthi, M. Kanagaraj, M. Kathiresan, V. Suryanarayanan and D. Velayutham, *J. Mater. Chem. A*, 2016, **4**, 4562–4569.

97 H. Luo, G. Wang, J. Lu, L. Zhuang and L. Xiao, *ACS Appl. Mater. Interfaces*, 2019, **11**, 41215–41221.

98 Y. J. Jang, S. Y. Kim, Y. M. Kim, J. K. Lee and H. C. Moon, *Energy Storage Mater.*, 2021, **43**, 20–29.

99 Y. M. Kim, W. Y. Lee, W. Y. Choi and H. C. Moon, *J. Ind. Eng. Chem.*, 2020, **90**, 341–350.

100 Q. Tang, H. Li, Y. Yue, Q. Zhang, H. Wang, Y. Li and P. Chen, *Mater. Des.*, 2017, **118**, 279–285.

101 S. Y. Kim, Y. J. Jang, Y. M. Kim, J. K. Lee and H. C. Moon, *Adv. Funct. Mater.*, 2022, **32**, 2200757.

102 Y. Liu, I. Murtaza, A. Shuja and H. Meng, *Chem. Eng. J.*, 2020, **379**, 122326.

103 H. Zhang, M. Yao, J. Wei, Y. Zhang, S. Zhang, Y. Gao, J. Li, P. Lu, B. Yang and Y. Ma, *Adv. Energy Mater.*, 2017, **7**, 1701063.

104 Y. Dai, W. Li, Z. Chen, X. Zhu, J. Liu, R. Zhao, D. S. Wright, A. Noori, M. F. Mousavi and C. Zhang, *J. Mater. Chem. A*, 2019, **7**, 16397–16405.

105 W. Li, Y. Guo, J. Shi, H. Yu and H. Meng, *Macromolecules*, 2016, **49**, 7211–7219.

106 S. Ming, S. Zhen, K. Lin, L. Zhao, J. Xu and B. Lu, *ACS Appl. Mater. Interfaces*, 2015, **7**, 11089–11098.

107 G. Sonmez, C. K. F. Shen, Y. Rubin and F. Wudl, *Angew. Chem.*, 2004, **116**, 1524–1528.

108 S. Ming, S. Zhen, X. Liu, K. Lin, H. Liu, Y. Zhao, B. Lu and J. Xu, *Polym. Chem.*, 2015, **6**, 8248–8258.

109 W. Wang, B. Zhao, Z. Cong, Y. Xie, H. Wu, Q. Liang, S. Liu, F. Liu, C. Gao, H. Wu and Y. Cao, *ACS Energy Lett.*, 2018, **3**, 1499–1507.

110 J. Roncali, *Chem. Rev.*, 1992, **92**, 711–738.

111 G. A. Snook, P. Kao and A. S. Best, *J. Power Sources*, 2011, **196**, 1–12.

112 Y. Guo, W. Li, H. Yu, D. F. Perepichka and H. Meng, *Adv. Energy Mater.*, 2017, **7**, 1601623.

113 L. A. Estrada, D. Y. Liu, D. H. Salazar, A. L. Dyer and J. R. Reynolds, *Macromolecules*, 2012, **45**, 8211–8220.

114 S. Ming, C. Zhang, P. Jiang, Q. Jiang, Z. Ma, J. Song and Z. Bo, *ACS Appl. Mater. Interfaces*, 2019, **11**, 19444–19451.

115 Y. Liu, C. Zhang, D. Hao, Z. Zhang, L. Wu, M. Li, S. Feng, X. Xu, F. Liu, X. Chen and Z. Bo, *Chem. Mater.*, 2018, **30**, 4307–4312.

116 Q. Huang, J. Chen, S. Yan, X. Shao, Y. Dong, J. Liu, W. Li and C. Zhang, *ACS Sustainable Chem. Eng.*, 2021, **9**, 13807–13817.

117 L. Liu, M. Layani, S. Yellinek, A. Kamyshny, H. Ling, P. S. Lee, S. Magdassi and D. Mandler, *J. Mater. Chem. A*, 2014, **2**, 16224–16229.

118 M. Layani, P. Darmawan, W. L. Foo, L. Liu, A. Kamyshny, D. Mandler, S. Magdassi and P. S. Lee, *Nanoscale*, 2014, **6**, 4572–4576.

119 G. Cai, P. Darmawan, M. Cui, J. Wang, J. Chen, S. Magdassi and P. S. Lee, *Adv. Energy Mater.*, 2016, **6**, 1501882.

120 W. Liu, M.-S. Song, B. Kong and Y. Cui, *Adv. Mater.*, 2017, **29**, 1603436.

121 S. Gong and W. Cheng, *Adv. Energy Mater.*, 2017, **7**, 1700648.

122 T. An, Y. Ling, S. Gong, B. Zhu, Y. Zhao, D. Dong, L. W. Yap, Y. Wang and W. Cheng, *Adv. Mater. Technol.*, 2019, **4**, 1800473.

123 Y. Wang, S. Gong, D. Gómez, Y. Ling, L. W. Yap, G. P. Simon and W. Cheng, *ACS Nano*, 2018, **12**, 8717–8722.

124 S.-E. Chun, B. Evanko, X. Wang, D. Vonlanthen, X. Ji, G. D. Stucky and S. W. Boettcher, *Nat. Commun.*, 2015, **6**, 1–10.

125 X. Jiao, G. Li, Z. Yuan and C. Zhang, *ACS Appl. Energy Mater.*, 2021, **4**, 14155–14168.

126 W. Li, F. Yuan, N. Xu, S. Mei, Z. Chen and C. Zhang, *Electrochim. Acta*, 2021, **384**, 138344.

127 T. Ye, Y. Sun, X. Zhao, B. Lin, H. Yang, X. Zhang and L. Guo, *J. Mater. Chem. A*, 2018, **6**, 18994–19003.

128 X. Lv, J. Li, L. Zhang, M. Ouyang, A. Tameev, A. Nekrasov, G. Kim and C. Zhang, *Chem. Eng. J.*, 2022, **431**, 133733.

129 Y. Dai, W. Li, R. Zhao, Q. Huang, N. Xu, F. Yuan and C. Zhang, *Electrochim. Acta*, 2019, **318**, 322–332.

130 D. Wei, M. R. J. Scherer, C. Bower, P. Andrew, T. Ryhänen and U. Steiner, *Nano Lett.*, 2012, **12**, 1857–1862.

131 M. J. Parent, S. Passerini, B. B. Owens and W. H. Smyrl, *J. Electrochem. Soc.*, 1999, **146**, 1346.

132 T. Y. Yun, X. Li, S. H. Kim and H. C. Moon, *ACS Appl. Mater. Interfaces*, 2018, **10**, 43993–43999.

133 L. Shen, L. Du, S. Tan, Z. Zang, C. Zhao and W. Mai, *Chem. Commun.*, 2016, **52**, 6296–6299.

134 J. Kim, A. I. Inamdar, Y. Jo, S. Cho, A. T. A. Ahmed, B. Hou, S. Cha, T. Geun Kim, H. Kim and H. Im, *J. Mater. Chem. A*, 2020, **8**, 13459–13469.

135 J. A. Koza, E. W. Bohannan and J. A. Switzer, *ACS Nano*, 2013, **7**, 9940–9946.

136 Y. Jo, K. Jung, J. Kim, H. Woo, J. Han, H. Kim, J. Hong, J.-K. Lee and H. Im, *Sci. Rep.*, 2014, **4**, 1–7.

137 J. Chen, Z. Wang, Z. Chen, S. Cong and Z. Zhao, *Nano Lett.*, 2020, **20**, 1915–1922.

138 K.-W. Kim, T. Y. Yun, S.-H. You, X. Tang, J. Lee, Y. Seo, Y.-T. Kim, S. H. Kim, H. C. Moon and J. K. Kim, *NPG Asia Mater.*, 2020, **12**, 1–10.

139 S. Y. Kim, T. Y. Yun, K. S. Yu and H. C. Moon, *ACS Appl. Mater. Interfaces*, 2020, **12**, 51978–51986.

140 L. Liu, X. Diao, Z. He, Y. Yi, T. Wang, M. Wang, J. Huang, X. He, X. Zhong and K. Du, *Energy Storage Mater.*, 2020, **33**, 258–267.

141 J. Xue, W. Li, Y. Song, Y. Li and J. Zhao, *J. Alloys Compd.*, 2021, **857**, 158087.

142 S. Zhou, S. Wang, S. Zhou, H. Xu, J. Zhao, J. Wang and Y. Li, *Nanoscale*, 2020, **12**, 8934–8941.

143 S. Wang, H. Xu, T. Hao, M. Xu, J. Xue, J. Zhao and Y. Li, *Appl. Surf. Sci.*, 2022, **577**, 151889.

144 D. Mohanadas, N. H. N. Azman and Y. Sulaiman, *J. Energy Storage*, 2022, **48**, 103954.

145 M. Zhu, Y. Huang, Y. Huang, W. Meng, Q. Gong, G. Li and C. Zhi, *J. Mater. Chem. A*, 2015, **3**, 21321–21327.

146 Q. Guo, J. Li, B. Zhang, G. Nie and D. Wang, *ACS Appl. Mater. Interfaces*, 2019, **11**, 6491–6501.

147 D. V. Zhuzhelskii, E. G. Tolstopjatova, S. N. Eliseeva, A. V. Ivanov, S. Miao and V. V. Kondratiev, *Electrochim. Acta*, 2019, **299**, 182–190.

148 X. Xia, D. Chao, X. Qi, Q. Xiong, Y. Zhang, J. Tu, H. Zhang and H. J. Fan, *Nano Lett.*, 2013, **13**, 4562–4568.

149 Z. Li, B. Wang, X. Zhao, Q. Guo and G. Nie, *New J. Chem.*, 2020, **44**, 20584–20591.

150 Q. Guo, X. Zhao, Z. Li, D. Wang and G. Nie, *Chem. Eng. J.*, 2020, **384**, 123370.

151 J. Li, Q. Guo, Y. Lu and G. Nie, *Eur. Polym. J.*, 2019, **113**, 29–35.

152 A. I. Inamdar, J. Kim, Y. Jo, H. Woo, S. Cho, S. M. Pawar, S. Lee, J. L. Gunjakar, Y. Cho, B. Hou, S. Cha, J. Kwak, Y. Park, H. Kim and H. Im, *Sol. Energy Mater. Sol. Cells*, 2017, **166**, 78–85.

153 K. S. Kumar, N. Choudhary, Y. Jung and J. Thomas, *ACS Energy Lett.*, 2018, **3**, 482–495.

154 X. Peng, L. Peng, C. Wu and Y. Xie, *Chem. Soc. Rev.*, 2014, **43**, 3303–3323.

155 M. Hu, H. Zhang, T. Hu, B. Fan, X. Wang and Z. Li, *Chem. Soc. Rev.*, 2020, **49**, 6666–6693.

156 M. Boota, M. Rajesh and M. Bécuwe, *Mater. Today Energy*, 2020, **18**, 100532.

157 J. Li, A. Levitt, N. Kurra, K. Juan, N. Noriega, X. Xiao, X. Wang, H. Wang, H. N. Alshareef and Y. Gogotsi, *Energy Storage Mater.*, 2019, **20**, 455–461.

158 S. Mondal, Y. Ninomiya and M. Higuchi, *ACS Appl. Energy Mater.*, 2020, **3**, 10653–10659.

159 S. Mondal, Y. Ninomiya, T. Yoshida, T. Mori, M. K. Bera, K. Ariga and M. Higuchi, *ACS Appl. Mater. Interfaces*, 2020, **12**, 31896–31903.

160 S. Mondal, T. Yoshida, S. Maji, K. Ariga and M. Higuchi, *ACS Appl. Mater. Interfaces*, 2020, **12**, 16342–16349.

161 G. Cai, J. Chen, J. Xiong, A. Lee-Sie Eh, J. Wang, M. Higuchi and P. S. Lee, *ACS Energy Lett.*, 2020, **5**, 1159–1166.

162 O. Eisenberg, Y. M. Algavi, H. Weissman, J. Narevicius, B. Rybtchinski, M. Lahav and M. E. van der Boom, *Adv. Mater. Interfaces*, 2020, **7**, 2000718.

163 P. Zhang, F. Zhu, F. Wang, J. Wang, R. Dong, X. Zhuang, O. G. Schmidt and X. Feng, *Adv. Mater.*, 2017, **29**, 1604491.

164 J. Lin, Z. Peng, Y. Liu, F. Ruiz-Zepeda, R. Ye, E. L. G. Samuel, M. J. Yacaman, B. I. Yakobson and J. M. Tour, *Nat. Commun.*, 2014, **5**, 1–8.

165 J. Lin, C. Zhang, Z. Yan, Y. Zhu, Z. Peng, R. H. Hauge, D. Natelson and J. M. Tour, *Nano Lett.*, 2013, **13**, 72–78.

166 W. Liu, C. Lu, X. Wang, R. Y. Tay and B. K. Tay, *ACS Nano*, 2015, **9**, 1528–1542.

167 T. G. Yun, M. Park, D.-H. Kim, D. Kim, J. Y. Cheong, J. G. Bae, S. M. Han and I.-D. Kim, *ACS Nano*, 2019, **13**, 3141–3150.

168 Z. Bi, X. Li, Y. Chen, X. He, X. Xu and X. Gao, *ACS Appl. Mater. Interfaces*, 2017, **9**, 29872–29880.

169 R. T. Ginting, M. M. Ovhal and J.-W. Kang, *Nano Energy*, 2018, **53**, 650–657.

170 T. G. Yun, D. Kim, Y. H. Kim, M. Park, S. Hyun and S. M. Han, *Adv. Mater.*, 2017, **29**, 1606728.

171 S. Topal, O. Savlug Ipek, E. Sezer and T. Ozturk, *Chem. Eng. J.*, 2022, **434**, 133868.

172 H. Peng, B. Yan, M. Jiang, B. Liu, Y. Gu, G. Yao, Y. Zhang, L. Ye, X. Bai and S. Chen, *J. Mater. Chem. A*, 2021, **9**, 1669–1677.

173 L. Liu, T. Wang, Z. He, Y. Yi, M. Wang, Z. Luo, Q. Liu, J. Huang, X. Zhong, K. Du and X. Diao, *Chem. Eng. J.*, 2021, **414**, 128892.

174 S. Zhang, S. Chen, Y. Cao, F. Yang, H. Peng, B. Yan, H. Jiang, Y. Gu and M. Xiang, *J. Mater. Sci.: Mater. Electron.*, 2019, **30**, 13497–13508.

175 D. Mohanadas, N. H. N. Azman, J. Abdullah, N. A. Endot and Y. Sulaiman, *Ceram. Int.*, 2021, **47**, 34529–34537.

176 P. Yao, S. Xie, M. Ye, R. Yu, Q. Liu, D. Yan, W. Cai, W. Guo and X. Yang Liu, *RSC Adv.*, 2017, **7**, 29088–29095.

177 W. Xinming, W. Qiguan, Z. Wenzhi, W. Yan and C. Weixing, *J. Mater. Sci.*, 2016, **51**, 7731–7741.

178 N. O. Laschuk, I. I. Ebralidze, E. B. Easton and O. V. Zenkina, *ACS Appl. Energy Mater.*, 2021, **4**, 3469–3479.

179 K. Li, Y. Shao, S. Liu, Q. Zhang, H. Wang, Y. Li and R. B. Kaner, *Small*, 2017, **13**, 1700380.

180 N. Nitta, F. Wu, J. T. Lee and G. Yushin, *Mater. Today*, 2015, **18**, 252–264.

181 M. Winter, B. Barnett and K. Xu, *Chem. Rev.*, 2018, **118**, 11433–11456.

182 H. Li, *Joule*, 2019, **3**, 911–914.

183 Y. Ding, Q. Deng, C. You, Y. Xu, J. Li and B. Xiao, *Phys. Chem. Chem. Phys.*, 2020, **22**, 21208–21221.

184 G. Li, B. Zhang, J. Wang, H. Zhao, W. Ma, L. Xu, W. Zhang, K. Zhou, Y. Du and G. He, *Angew. Chem., Int. Ed.*, 2019, **58**, 8468–8473.

185 W. C. Poh, X. Gong, F. Yu and P. S. Lee, *Adv. Sci.*, 2021, **8**, 2101944.

186 C. Wang, Z. Wang, Y. Ren, X. Hou and F. Yan, *ACS Sustainable Chem. Eng.*, 2020, **8**, 5050–5055.

187 V. D. Neff, *J. Electrochem. Soc.*, 1985, **132**, 1382.

188 D. E. McCoy, T. Feo, T. A. Harvey and R. O. Prum, *Nat. Commun.*, 2018, **9**, 1–8.

189 N. Zhang, F. Cheng, Y. Liu, Q. Zhao, K. Lei, C. Chen, X. Liu and J. Chen, *J. Am. Chem. Soc.*, 2016, **138**, 12894–12901.

190 W. Zhang, H. Li, M. Al Hussein and A. Y. Elezzabi, *Adv. Opt. Mater.*, 2020, **8**, 1901224.

191 H. Li, L. McRae, C. J. Firby and A. Y. Elezzabi, *Adv. Mater.*, 2019, **31**, 1807065.

192 Z. Tong, T. Kang, Y. Wan, R. Yang, Y. Wu, D. Shen, S. Liu, Y. Tang and C. Lee, *Adv. Funct. Mater.*, 2021, **31**, 2104639.

193 Z. Tong, R. Lian, R. Yang, T. Kang, J. Feng, D. Shen, Y. Wu, X. Cui, H. Wang, Y. Tang and C.-S. Lee, *Energy Storage Mater.*, 2022, **44**, 497–507.

194 B. Yang, D. Ma, E. Zheng and J. Wang, *Sol. Energy Mater. Sol. Cells*, 2019, **192**, 1–7.

195 J. Wang, J. Liu, M. Hu, J. Zeng, Y. Mu, Y. Guo, J. Yu, X. Ma, Y. Qiu and Y. Huang, *J. Mater. Chem. A*, 2018, **6**, 11113–11118.

196 B. Sun, Z. Liu, W. Li, H. Huang, Y. Xia, Y. Gan, C. Liang, W. Zhang and J. Zhang, *Sol. Energy Mater. Sol. Cells*, 2021, **231**, 111314.

197 S. B. Singh, D. T. Tran, K. Jeong, N. H. Kim and J. H. Lee, *Small*, 2022, **18**, 2104462.

198 H. Li, C. J. Firby and A. Y. Elezzabi, *Joule*, 2019, **3**, 2268–2278.

199 H. Li and A. Y. Elezzabi, *Nanoscale Horiz.*, 2020, **5**, 691–695.

200 X. Xu, M. Duan, Y. Yue, Q. Li, X. Zhang, L. Wu, P. Wu, B. Song and L. Mai, *ACS Energy Lett.*, 2019, **4**, 1328–1335.

201 B. Ji, H. He, W. Yao and Y. Tang, *Adv. Mater.*, 2021, **33**, 2005501.

202 J. Zhang, J. Yang, G. Leftheriotis, H. Huang, Y. Xia, C. Liang, Y. Gan and W. Zhang, *Electrochim. Acta*, 2020, **345**, 136235.

203 S. R. Anton and H. A. Sodano, *Smart Mater. Struct.*, 2007, **16**, 1–21.

204 S.-Y. Chang, P. Cheng, G. Li and Y. Yang, *Joule*, 2018, **2**, 1039–1054.

205 X. Xia, Z. Ku, D. Zhou, Y. Zhong, Y. Zhang, Y. Wang, M. Joon Huang, J. Tu and H. Jin Fan, *Mater. Horiz.*, 2016, **3**, 588–595.

206 D. Zhou, N. Wang, T. Yang, L. Wang, X. Cao and Z. Lin Wang, *Mater. Horiz.*, 2020, **7**, 2158–2167.

207 Z. Liu, J. Yang, G. Leftheriotis, H. Huang, Y. Xia, Y. Gan, W. Zhang and J. Zhang, *Sustain. Mater. Technol.*, 2022, **31**, 00372.

208 D. Zhang, B. Sun, H. Huang, Y. Gan, Y. Xia, C. Liang, W. Zhang and J. Zhang, *Materials*, 2020, **13**, 1206.

209 W. Guo, Z. Cong, Z. H. Guo, P. Zhang, Y. Chen, W. Hu, Z. L. Wang and X. Pu, *Adv. Funct. Mater.*, 2021, **31**, 2104348.

210 S. Qin, Q. Zhang, X. Yang, M. Liu, Q. Sun and Z. L. Wang, *Adv. Energy Mater.*, 2018, **8**, 1800069.

211 J. Cho, T. Y. Yun, H. Y. Noh, S. H. Baek, M. Nam, B. Kim, H. C. Moon and D. Ko, *Adv. Funct. Mater.*, 2020, **30**, 1909601.

212 F. Zhou, Z. Ren, Y. Zhao, X. Shen, A. Wang, Y. Y. Li, C. Surya and Y. Chai, *ACS Nano*, 2016, **10**, 5900–5908.

213 Z. Yang, L. Li, Y. Luo, R. He, L. Qiu, H. Lin and H. Peng, *J. Mater. Chem. A*, 2012, **1**, 954–958.

214 R. Liu, Y. Liu, H. Zou, T. Song and B. Sun, *Nano Res.*, 2017, **10**, 1545–1559.